AD A051933

ARBRL-MR-02807

AD E400 112

AD

(12)

BRL

MEMORANDUM REPORT ARBRL-MR-02807

A COMPARISON OF COMPUTED VERSUS
EXPERIMENTAL LOADING AND RESPONSE OF
A FLAT PLATE SUBJECTED TO MINE BLAST

Richard E. Lottero
Kent D. Kimsey

January 1978

DDC

RECEIVED

MAR 30 1978

B

USA ARMAMENT RESEARCH AND DEVELOPMENT COMMAND
USA BALLISTIC RESEARCH LABORATORY
ABERDEEN PROVING GROUND, MARYLAND

DDC FILE COPY

Destroy this report when it is no longer needed.
Do not return it to the originator.

The findings in this report are not to be construed as
an official Department of the Army position, unless
so designated by other authorized documents.

*The use of trade names or manufacturers' names in this report
does not constitute indorsement of any commercial product.*

SECURITY CLASSIFICATION OF THIS PAGE (When Data Entered)

REPORT DOCUMENTATION PAGE

READ INSTRUCTIONS BEFORE COMPLETING FORM

1. REPORT NUMBER	2. GOVT ACCESSION NO.	3. RECIPIENT'S CATALOG NUMBER
MEMORANDUM REPORT ARBRL-MR-02807		

4. TITLE (and Subtitle)

A COMPARISON OF COMPUTED VERSUS EXPERIMENTAL LOADING AND RESPONSE OF A FLAT PLATE SUBJECTED TO MINE BLAST.

5. TYPE OF REPORT & PERIOD COVERED

Final rept.
1 Oct 75 - 31 Dec 76

6. PERFORMING ORG. REPORT NUMBER

7. AUTHOR(s)

Richard E. Lottero
Kent D. Kimsey

8. CONTRACT OR GRANT NUMBER(s)

9. PERFORMING ORGANIZATION NAME AND ADDRESS

US Army Ballistic Research Laboratory
(ATTN: DRDAR-BLT)
Aberdeen Proving Ground, MD 21005

10. PROGRAM ELEMENT, PROJECT, TASK AREA & WORK UNIT NUMBERS

1T662618AH80 - Work Unit 0XJ
2618A - Task Area 01

11. CONTROLLING OFFICE NAME AND ADDRESS

US Army Armament Research & Development Command
US Army Ballistic Research Laboratory
(ATTN: DRDAR-BL)
Aberdeen Proving Ground, MD 21005

12. REPORT DATE

JAN 78

13. NUMBER OF PAGES

59

14. MONITORING AGENCY NAME & ADDRESS(if different from Controlling Office)

15. SECURITY CLASS. (of this report)

Unclassified

15a. DECLASSIFICATION/DOWNGRADING SCHEDULE

16. DISTRIBUTION STATEMENT (of this Report)

Approved for public release; distribution unlimited.

17. DISTRIBUTION STATEMENT (of the abstract entered in Block 20, if different from Report)

18. SUPPLEMENTARY NOTES

19. KEY WORDS (Continue on reverse side if necessary and identify by block number)

Buried Land Mine
Mine Blast
Hydrocode
Structural Response Code
Armor Plate Response

Soil Modeling

20. ABSTRACT (Continue on reverse side if necessary and identify by block number) (ljc)

The DORF hydrocode is used to generate the loading history on a target plate subjected to the blast loading from a buried land mine. The REPSIL structural response code is used to compute the response of the target plate to this loading. The deflection of a clamped-edge, square, target plate of rolled homogeneous armor, 25.4 cm on a side and 0.678 cm thick, centered above a buried 0.265 kg charge of C-4, is predicted. The computations performed here are numerical simulations of a field experiment performed and reported by the Southwest Research Institute (SwRI). The agreement with the SwRI empirical

DD FORM 1473 EDITION OF 1 NOV 65 IS OBSOLETE

393 471.1

SECURITY CLASSIFICATION OF THIS PAGE (When Data Entered)

20.   (Cont'd)

correlation functions, which include the data for this field experiment, is
excellent: the DORF calculation for the total impulse delivered to the target
is 4.5% above the value computed using the SwRI correlation function for im-
pulse; the REPSIL calculation for the maximum residual deformation of the target
plate is 10% above the value computed using the SwRI correlation function for
maximum residual deformation. The remainder of the profile for the residual
deformation of the target plate shows even better agreement with the SwRI corre-
lation function.

TABLE OF CONTENTS

Page

LIST OF ILLUSTRATIONS

5

PRECEDING PAGE BLANK-NOT FILMED

LIST OF ILLUSTRATIONS (Continued)

6

LIST OF ILLUSTRATIONS (Continued)

I. INTRODUCTION

There is a continuing need for modeling the structural damage inflicted by mine blast on the undersides of tanks and other armored vehicles, for both vulnerability assessments and to rationally provide hardening for such vehicles. This has been a subject of long-standing interest at the Ballistic Research Laboratory and at other agencies at Aberdeen Proving Ground. A considerable number of tests have been performed and much field damage data gathered over the years[1-10]. In the recent past, an analytical approach has been reported[11].

---

[1]Hanna, J. W., "An Effectiveness Evaluation of Several Types of Antitank Mines," BRL-MR-616, US Army Ballistic Research Laboratory, Aberdeen Proving Ground, MD (June 1952). (AD #377342)

[2]Bailey, R. A., Born, D., and Sultanoff, M., "Analysis of the Performance of the Mock-Up Booster Assembly for the Multi-Jet, Shaped Charge, Anti-Tank Mine," BRL-MR-584, US Army Ballistic Research Laboratory, Aberdeen Proving Ground, MD (October 1951). (AD #377333)

[3]Haskell, D. F. and Reisinger, M. J., "Armored Vehicle Vulnerability Analysis Model - First Version, Introduction," BRL-R-1857, US Army Ballistic Research Laboratory, Aberdeen Proving Ground, MD (February 1976). (AD #B009638L)

[4]Clark, E. L., "Testing of Anti-Armor Devices," BRL-CR-221, US Army Ballistic Research Laboratory, Aberdeen Proving Ground, MD (April 1975). (AD #B003825L)

[5]Norman, R. M., "An Estimate of the Performance of the FRG Pandora Anti-Tank Mine" (U), BRL-MR-1754, US Army Ballistic Research Laboratory, Aberdeen Proving Ground, MD (July 1966) (SECRET-NOFORN). (AD #376685)

[6]Cioffi, A. R. and Vincent, A. R., "Preliminary Estimates of the Vulnerability of Light Weight Armored Vehicles to Attack by Antitank Mines," (U), BRL-TN-1197, US Army Ballistic Research Laboratory, Aberdeen Proving Ground, MD (June 1958) (CONFIDENTIAL). (AD #378697)

[7]Norman, R. M., "An Estimate of the Performance of the XM34 Anti-Tank Mine" (U), BRL-MR-1774, US Army Ballistic Research Laboratory, Aberdeen Proving Ground, MD (August 1966) (CONFIDENTIAL).

[8]Norman, R. M. and Beichler, G. P., "Effectiveness Studies of the XM34 AT Mine" (U), BRL-TN-1640, US Army Ballistic Research Laboratory, Aberdeen Proving Ground, MD (December 1966) (CONFIDENTIAL). (AD #379091)

[9]Norman, R. M. and Beichler, G. P., "An Estimate of the Performance of Buried XM34 Antitank Mines" (U), BRL-TN-1641, US Army Ballistic Research Laboratory, Aberdeen Proving Ground, MD (December 1966) (CONFIDENTIAL). (AD #379839)

[10]Norman, R. M., "Deformation in Flat Plates Exposed to HE Mine Blast," AMSAA-TM-74, US Army Materiel Systems Analysis Agency, Aberdeen Proving Ground, MD (May 1970).

[11]Haskell, D. F., "Deformation and Fracture of Tank Bottom Hull Plates Subjected to Mine Blast," BRL-R-1587, US Army Ballistic Research Laboratory, Aberdeen Proving Ground, MD (May 1972). (AD #901628)

More recently, preliminary computations, using the two-dimensional Eulerian, hydrodynamic computer code DORF[12], of the time-history of the loading of a rigid plate by a bare, spherical charge have been performed[13]. The DORF hydrocode uses a centered, finite difference technique to solve the unsteady Euler equations; it has an artificial viscosity option. These calculations were performed to determine the applicability of the DORF hydrocode to this problem, and to gain some insight as to the effect of the computational mesh on the solution. The bare charge computations treat both the air and the explosive products as polytropic gases, with the explosive being represented by a sphere of high-pressure quiescent explosive products initially resting tangent to a reflecting bottom boundary. The top boundary is also reflective, representing a rigid, fixed, target plate. Computational studies[14] using the DORF code indicate that the target plate loading using this representation of the explosive at initiation does not materially differ from that computed by using Taylor's[15] solution for the detonation wave. The intent of the present study is to use the experience gained from the previous work[13,14] to attempt to compute the target plate loading and deformation due to the blast from a land mine buried in soil, thereby also testing the ability of the DORF code to model a soil cover.

A recent study[16] at the Southwest Research Institute, hereafter referred to as SwRI, involves the collation of existing data for scaled experiments involving the encounter of buried land mines with various targets, and also reports new data for a series of small scale experiments, involving flat plates, performed by SwRI. A correlation function, based on the use of dimensional analysis, for the total impulse delivered by the land mine and overburden on a target is presented. For the special case wherein the target is an initially flat plate, the report also presents a function which relates the strain energy stored in the plate to the total energy delivered to the plate by the mine blast to compute the maximum residual deformation of the plate. This presents an opportunity to compare the integrated, experimental, total impulse, as computed using the SwRI correlation function, with that computed using the DORF hydrocode.

---

[12]Johnson, Wallace E., "Code Correlation Study,: AFWL-TR-70-144, Air Force Weapons Laboratory, Kirtland Air Force Base, NM (April 1971).

[13]Miller, James E., "Preliminary Study of Target Load Prediction by Use of a Hydrodynamic Computer Code," BRL MR-2472, US Army Ballistic Research Laboratory, Aberdeen Proving Ground, MD (April 1975). (AD B0038291.)

[14]Allison, W. D., BRL, private communication of as yet unpublished data.

[15]Taylor, Geoffrey I., Sir, The Dynamics of the Combustion Products behind Plane and Spherical Detonation Fronts in Explosives, Proceedings of the Royal Society of London, Series A, Vol. 200, 22 February 1950.

[16]Westine, Peter S. and Hokanson, James C., "Procedures to Predict Plate Deformations from Land Mine Explosions" (U), TACOM Technical Report No. 12049, US Army Tank Automotive Command, Warren, MI (August 1975) (CONFIDENTIAL).

Maximum residual deformation data for the SwRI test series using flat
plates are also reported[16], as is a function for the general shape of the
deformed plate. The loading generated by the DORF hydrocode is used as
input to the REPSIL[17] structural response code to compute the target plate
response. The computed response is then compared directly to the maximum
residual deformation and the general deformed shape which are predicted by
the SwRI correlation function.

II. SIMULATED SwRI TEST

The SwRI data which show the least amount of scatter on the impulse
correlation curve are the bulge plate tests. The SwRI bulge plate test[16]
selected for computer simulation, test number 36 in the test series for
flat, square plates with a charge buried directly below the plate center,
involves a square armor plate, 25.4 cm on a side and 0.678 cm thick,
centered above a 0.265 kg charge of C-4. The total stand-off distance,
the distance from the bottom of the target plate to the center of the
charge, is 16.2 cm, of which 8.9 cm is the air gap between the overburden
and the target plate. In the experiment, the target plate is restrained
by a heavy collar; however, the collar is not massive enough to prevent
the plate and collar from being thrown several feet in the air by the
exploding land mine.

The high-explosive C-4 charge is of a pancake shape, with an assumed
thickness-to-diameter ratio of 5/13. The thickness-to-diameter ratio for
the charge used in this test was not reported[16]. There were references in
the text to this 5/13 ratio, and a photograph of a pancake charge to be
used for a bulge plate test indicated such ratio would be a reasonable
assumption. Assuming a normal density of 1.592 g/cm^3, the radius of the
charge is 4.1 cm, the thickness 3.2 cm. The distance from the soil sur-
face to the top of the charge is 5.7 cm.

The geometry of the problem allows the use of a cylindrical coordinate
system in the hydrocode calculation. The flow field prior to the detona-
tion of the charge is shown in Figure 1a. The left boundary of the flow
field is the axis of symmetry. The right and bottom boundaries are trans-
missive boundaries, far enough removed from the charge and the top boundary
so that artificial reflections from these boundaries do not have time to
invalidate the near-field solution at the top boundary. The computation
was stopped and analyzed frequently, so that any flow phenomena that did
not seem to have a physical basis could be identified, and their impact
on the solution evaluated. The top boundary is a rigid, immobile,
reflecting boundary, intended to simulate the target plate. This repre-
sentation of the target plate is a concession to the DORF hydrocode,
replacing a finite, movable, and deformable plate-and-collar combination

---

[17]Santiago, J. M., Wisniewski, H. L., and Huffington, N. J., Jr., "A
User's Manual for the REPSIL Code," BRL Report 1744, US Army Ballistic
Research Laboratory, Aberdeen Proving Ground, MD (October 1974).
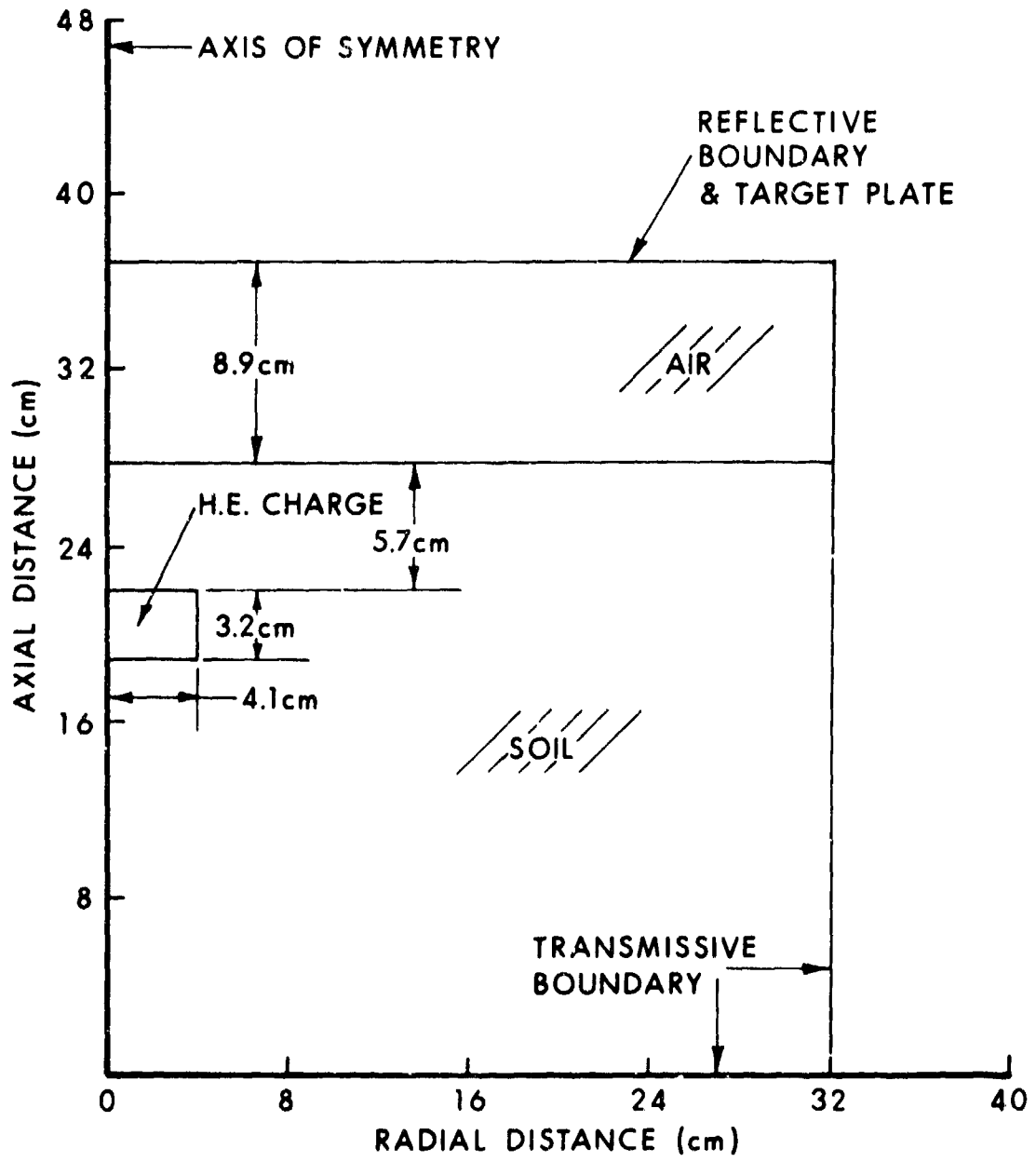(AD #A003176)

Figure 1a: The flow field at cycle 0, time = 0.

with an infinite, fixed, and rigid reflecting boundary. This concession simplifies the computational flow field considerably; it is believed to cause only a modest over-estimate of the forces on the plate, primarily by eliminating the possibility of computing rarefaction waves which would exist under experimental conditions.

The finite-difference computational grid for this use of the DORF hydrocode contains 60 flow field cells in the radial direction, with the vertical area projections of the cells increasing in a geometric progression with increasing radius. There are 80 cells in the axial direction; the cell heights are determined by a series of geometric progressions centered on the high-explosive charge (see Figure 1b). Because the DORF hydrocode uses a centered-differencing technique assuming equal cell volumes, it is assumed that the radial progression in cell volume used for this grid introduces less error than a radial progression in differential radius.

III. EQUATIONS OF STATE

Both the air and the explosive products are assumed to be polytropic gases[13,14], governed by the equation of state

$$p = \rho I (\gamma - 1),$$ (1)

where p represents pressure, ρ represents density, I represents specific internal energy, and γ represents the ratio of specific heats. For the air,

$$\gamma_a = 1.4,$$ (2.1)

and, for the explosive products[13,14],

$$\gamma_e = 2.71.$$ (2.2)

The soil surrounding the explosive products is governed by the Tillotson equation of state[18,19] as used by Johnson in the DORF[12] code, where the equation for the pressure takes on three main forms. The pressure in the compressed state, or any cold state, is

$$P_C = \left[a + \frac{b}{\frac{I}{I_0 \eta^2} + 1} \right] I\rho + A\mu + B\mu^2,$$ (3.1)

[18]Tillotson, J. H., "Metallic Equations of State for Hypervelocity Impact," GA-3216, General Atomic, Division of General Dynamics, San Diego, CA (July 1962).

[19]Hill, L. R. and Johnson, W. E., "Energy Partitioning during Hypervelocity Impact on Rocks," SC-R-70-4402, Sandia Laboratories, Albuquerque, NM (December 1970).
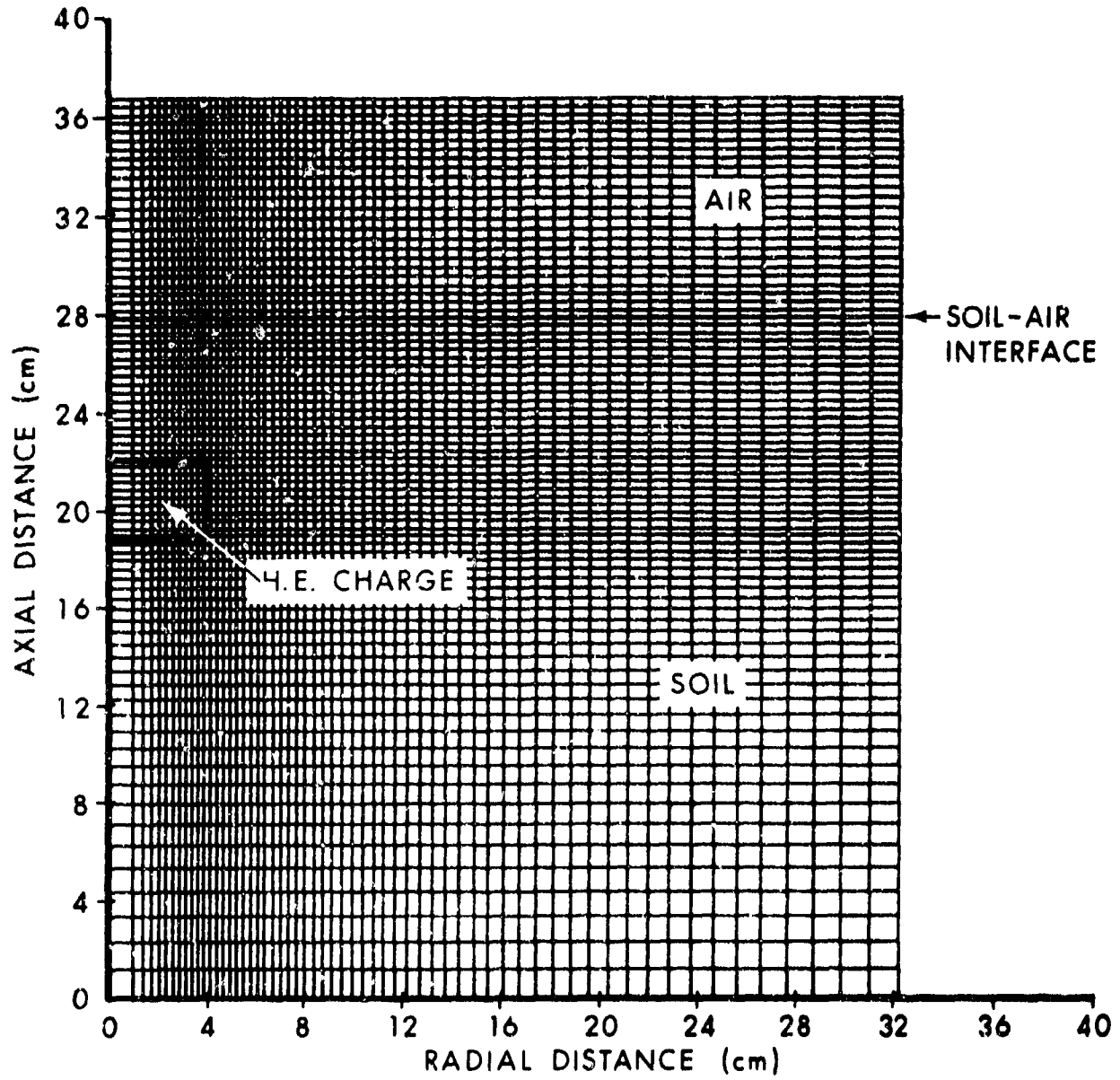
Figure 1b: The computational grid, with the
flow field at time = 0 superimposed.

14

where either

$$\eta > 1.0,$$

or

$$I < I_s,$$

or both.

The pressure for hot, expanded states is

$$P_E = aI\rho + \left[\frac{bI\rho}{\frac{I}{I_0\eta^2} + 1} + A\mu e^{-\alpha\left(\frac{\rho_0}{\rho} - 1\right)} \right] e^{-\beta\left(\frac{\rho_0}{\rho} - 1\right)^2}, \quad (3.2)$$

where

$$\eta < 1.0$$

and

$$I \geqslant I_s{'}.$$

The pressure for the transition state is

$$P_T = \frac{P_E\ (I-I_s) + P_C\ (I_s{'}-I)}{I_s{'}-I_s}, \quad (3.3)$$

where

$$\eta < 1.0$$

and

$$I_s \leqslant I < I_s{'}.$$

In the above equations,

$$\eta \equiv \frac{\rho}{\rho_0}, \quad (3.4)$$

and

$$\mu \equiv \eta - 1. \quad (3.5)$$

In the above equations, I_0 is the reference specific internal energy, I_s is the specific internal energy of the material as it is brought to the vaporization temperature, I_s' is equal to I_s plus the latent heat of vaporization for that material, and ρ_0 represents the reference density. The other parameters, a, b, A, B, α, and β, are input constants used for fitting the Tilloston equation of state to the selected material, and do not represent physical quantities.

The material assumed to represent the soil is dry tuff[20], with a water content less than or equal to 5 per cent by weight. While some soil properties for the test are reported by Westine and Hokanson[16], there are not enough to completely define the type, state, and properties of that soil. The soil and soil properties assumed here represent a best estimate, based on the information provided[16], and on consultations with W. E. Johnson[21], the originator of the DORF code. The constants for this assumed material[21] are:

$$a = 0.5,$$

$$b = 1.3,$$

$$A = 4.5 \text{ GPa},$$

$$B = 3.0 \text{ GPa},$$

$$I_0 = 6.0 \text{ MJ/kg},$$

$$\alpha = 5.0,$$

$$\beta = 5.0,$$

$$I_s = 3.2 \text{ MJ/kg},$$

$$I_s' = 18.0 \text{ MJ/kg},$$

and

$$\rho_0 = 1.7 \text{ Mg/m}^3.$$

[20]Allen, R. T., "Equation of State of Rocks and Minerals," GAMD 7834, General Atomic, Division of General Dynamics, San Diego, CA (March 1967).

[21]Johnson, W. E., Computer Code Consultants, Salona Beach, CA, private communication (November 1974).

IV. CALCULATION OF TARGET PLATE LOADS

As in the previous computations[13,14], the hydrocode computation is begun with the explosive being represented by a high-pressure, quiescent gas occupying the original volume of the explosive. A complete conversion of chemical to internal energy is assumed. At time zero, the pressure in the explosive products as computed by using Equation (1) with Equation (2.2) is 11.76 GPa, the pressure in the air is 100 kPa, and the soil is at zero stress. It would have been more precise to begin the problem with the soil at a compressive stress of 100 kPa; however, the error introduced is negligible: 100 kPa is insignificant as compared with the soil stresses caused by the explosion. Figure 2a shows the pressure in the computational flow field, plotted against both the radial and axial coordinates at 1.0 μs. The plotting program that produces these plots of pressure in the flow field plots the cell pressure at the upper right corner of the cell, rather than at the cell center, the actual location of the pressure value. This causes the plot to show an apparent gap along each axis. These two gaps are actually the first column, and first row, of cells. Figure 2b shows a spatial cut of pressure up the first column of flow field cells, also at 1.0 μs. Shocks have not yet formed at this early time, although the axial movement of the expansion waves into the high-pressure explosive products is evident. Figures 3a and 3b show similar plots at 3.2 μs. At this early time, shocks are well developed, the expanding explosive products initially causing planar shock waves to develop axially, and a cylindrical shock wave to develop radially. Pressure plots for the computational flow field show that these shock waves gradually merge to form a nearly spherical shock in the soil. The shock front expands unimpeded into the soil until the contact surface between the soil and the air is reached. Analysis of the DORF computation indicates that the shock wave first meets the soil-air contact surface at 17.1 μs in the innermost radial cell, the point of intersection of the shock wave and contact surface moving out radially thereafter. The incident shock in this innermost cell is still strong, the peak pressure at the time of arrival at the soil-air contact surface being 5.2 GPa. A strong expansion wave is reflected back into the soil, and a relatively weak shock wave, whose peak pressure is on the order of 1.0 MPa, is transmitted into the air. As the point of intersection of the incident shock wave with the soil-air contact surface moves radially outward, the soil bulges up behind it, traveling at relatively high speed toward the target plate.

The computation indicates that the computational air shock first strikes the top boundary at 85 μs, the reflected air shock in the innermost radial cell at the top boundary reaching a peak pressure of 4.4 MPa at 93 μs, as shown in Figure 4a; the soil first arrives at this cell at 112 μs, reaching a peak pressure of 1.0 GPa at 119 μs. Figure 4b shows the pressure in the computational flow field at 128 μs, shortly after the peak pressure has been reached in the inner-most radial cell at the top boundary. The point of peak pressure on the top boundary is moving out radially, and the pressure in the cells interior to that peak is relieving as the soil reflects off the top boundary. This may be seen in
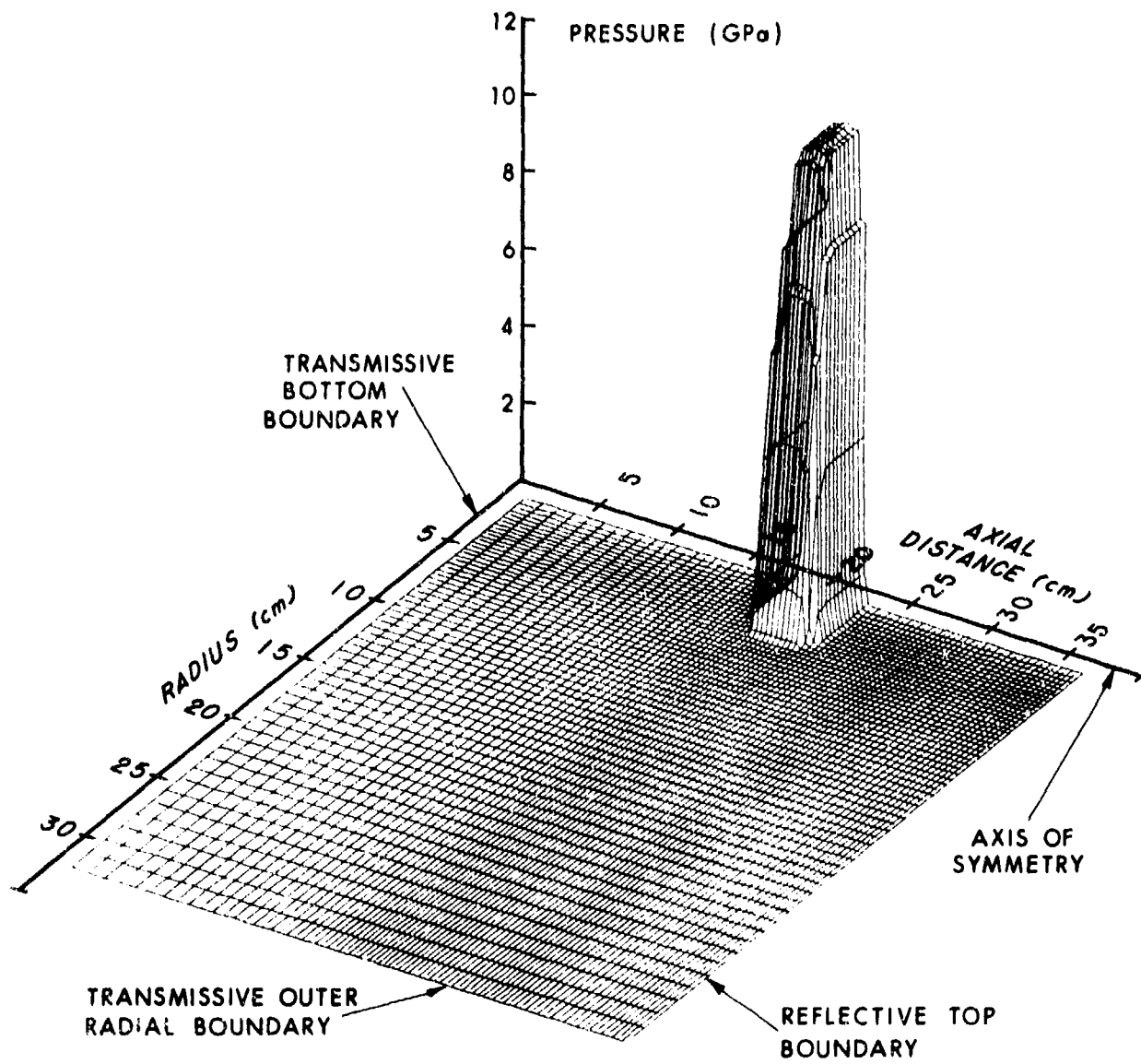
17

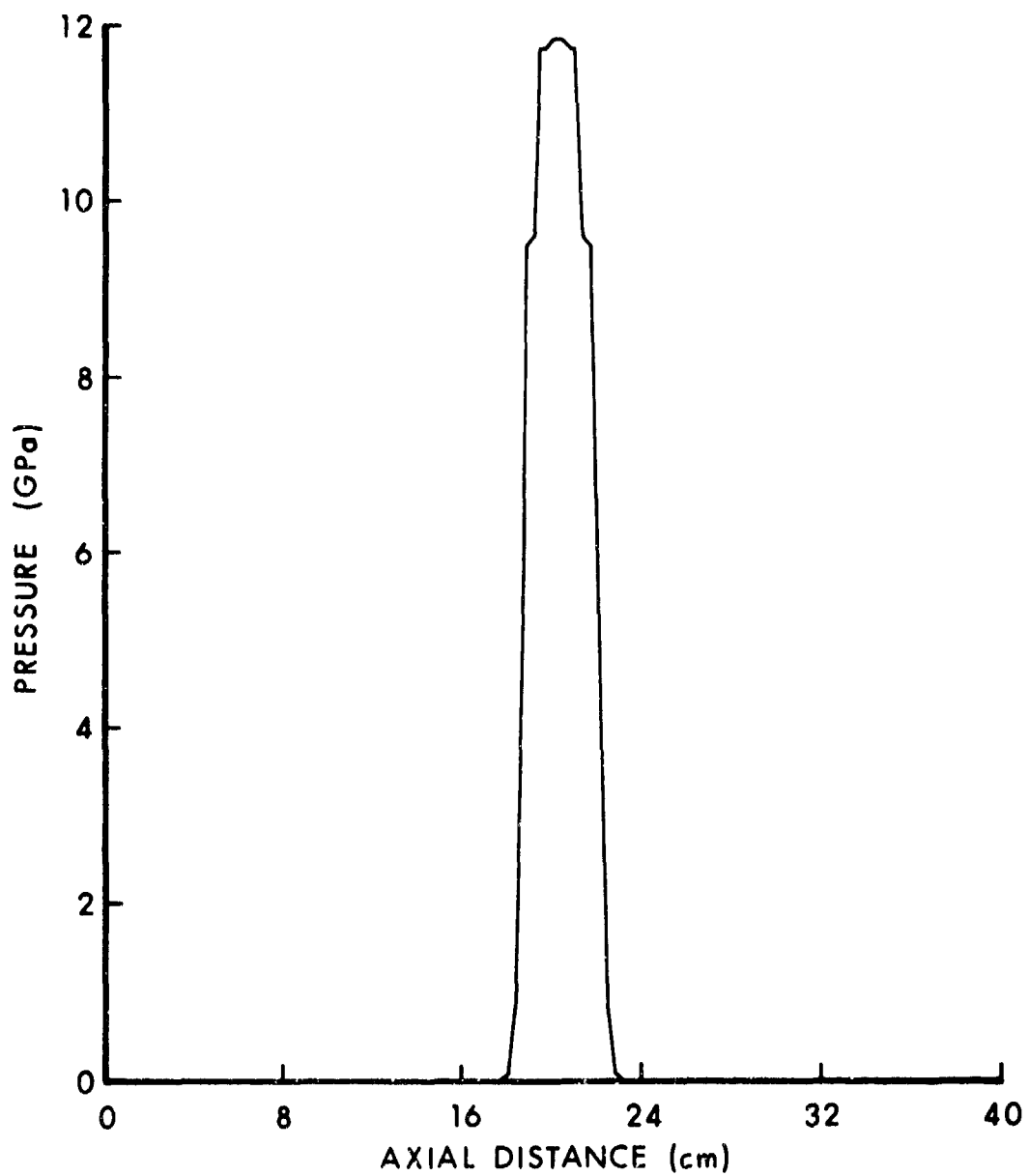Figure 2a: The pressure in the computational flow field at 1.0 μs.

Figure 2b: Spatial cut of pressure, first
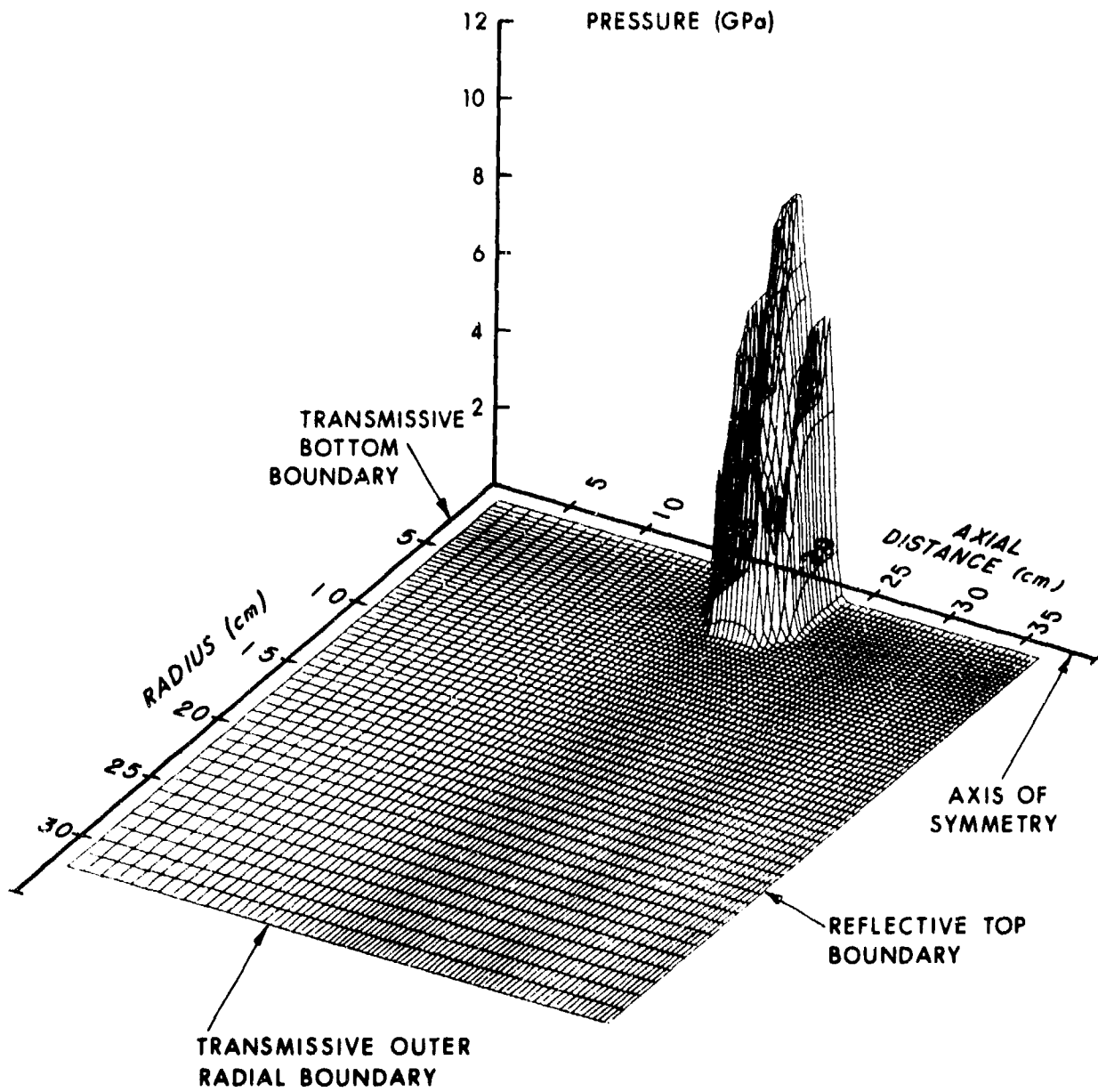column of cells along the axis of symmetry,
1.0 µs. No shocks are evident.

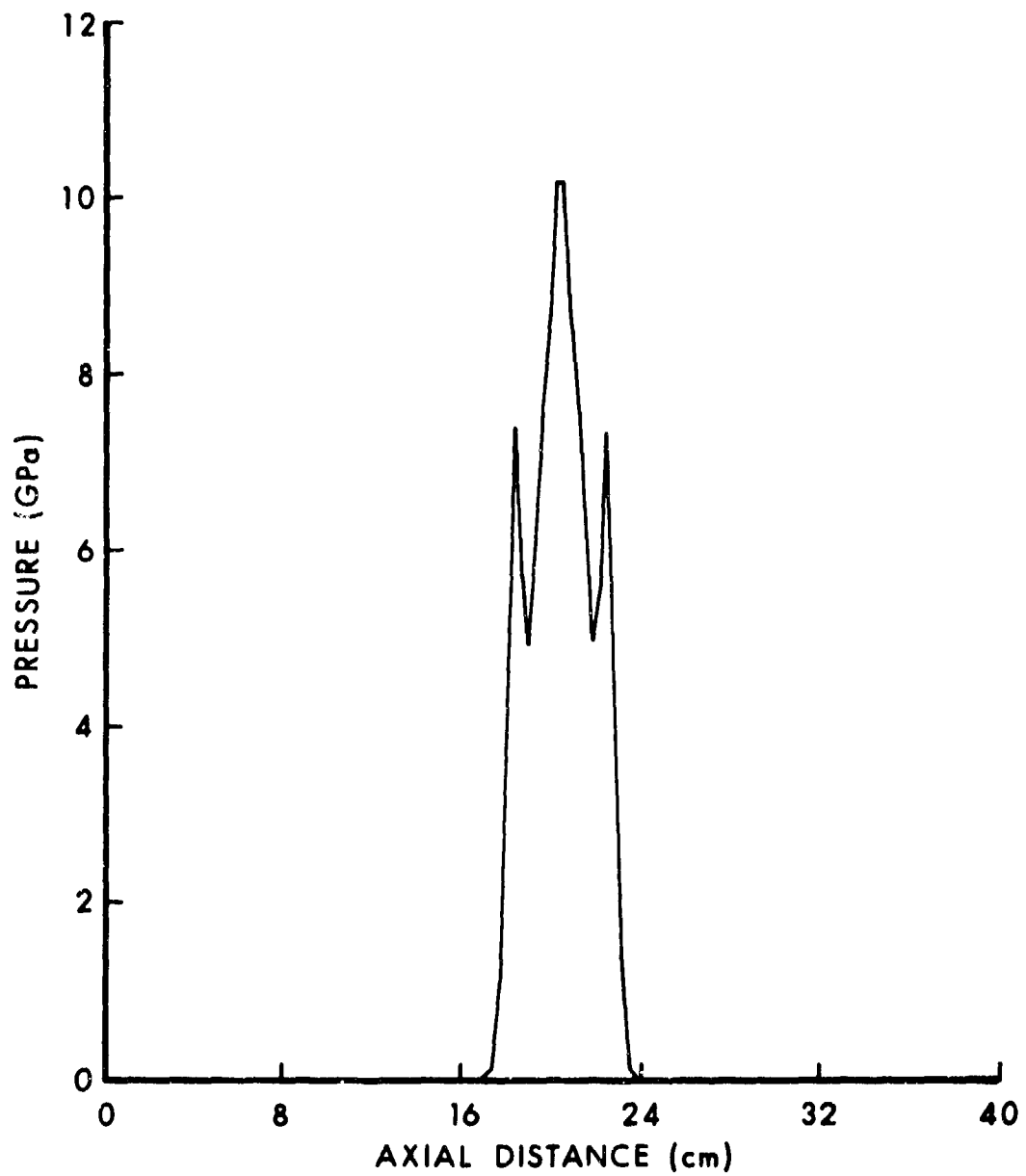Figure 3a: The pressure in the computational flow field at 3.2 µs.

Figure 3b: Spatial cut of pressure, first column
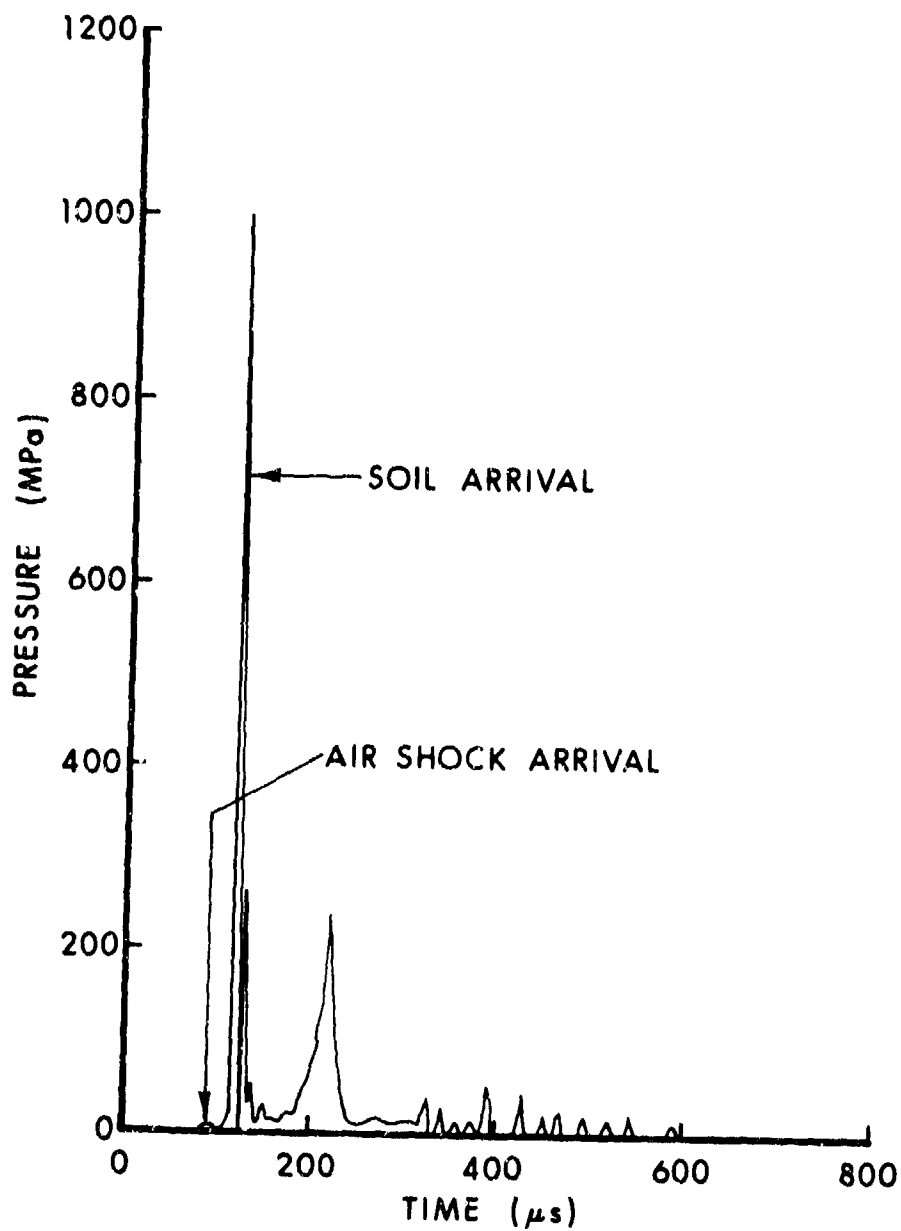of cells along the axis of symmetry,
3.2 μs. Shocks have formed.

21

Figure 4a: The pressure-time history in the inner-most radial cell on the top boundary.

22
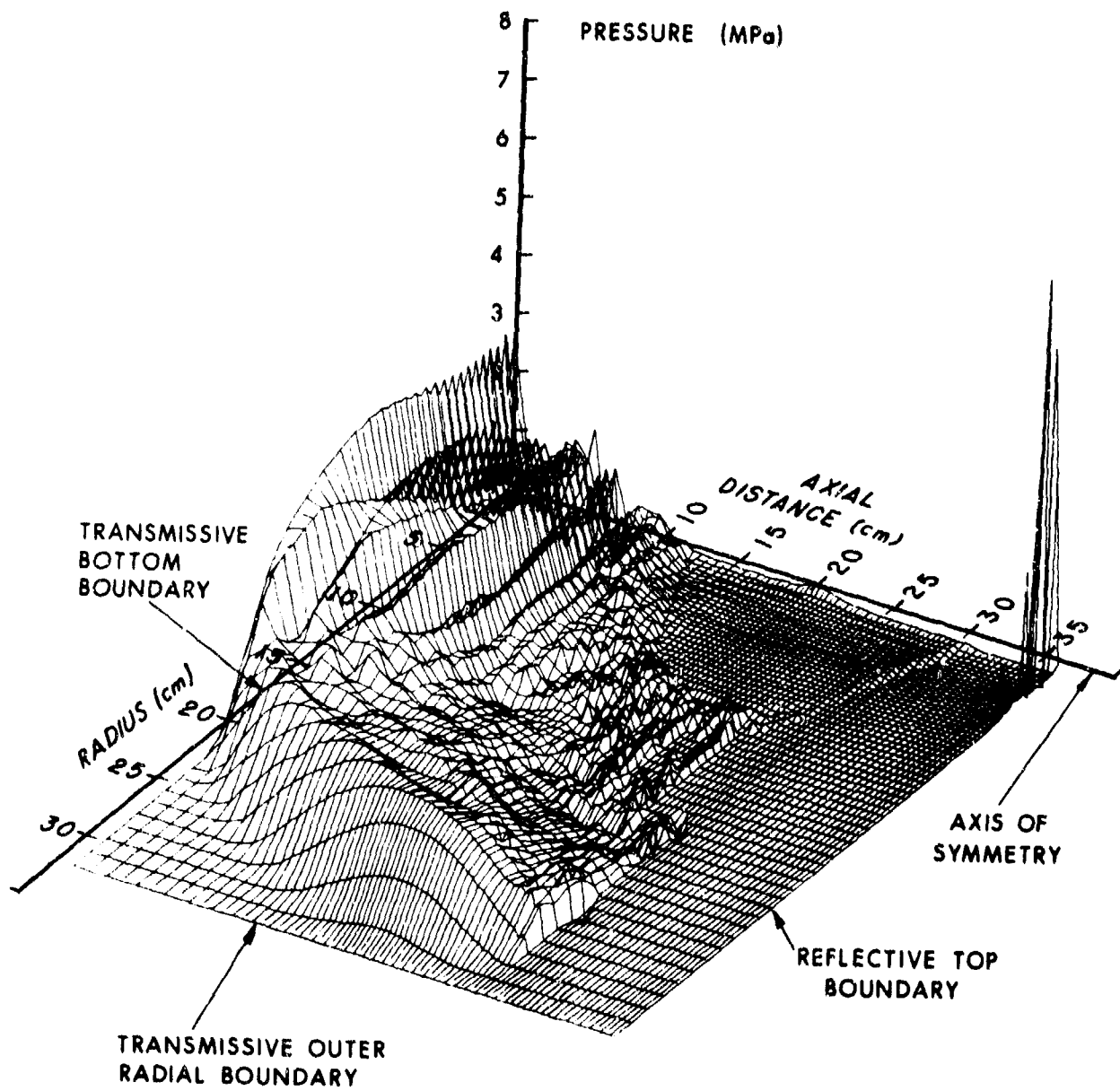
Figure 4b: The pressure in the computational flow field at 128 μs.

Figure 4c, a plot of pressure versus radius at the top boundary. In part, the jaggedness of this pressure plot may be due to computational, and not real, phenomena, as is common in explicit-time-step, Eulerian hydrocodes in which artificial viscosity is not invoked, as in the case for this computation. Figure 4d shows a spatial cut of pressure along the first column of cells along the axis. The shock wave in the soil has already passed through the bottom boundary of the grid. Although the bottom boundary is designed to be transmissive, a shock is reflected back up the grid. The pressure behind the incident shock at the bottom boundary is on the order of 0.6 GPa. The reflected wave, at 128 µs, is centered at an axial distance of 6 cm, with a peak pressure of 0.17 GPa, and is about to strike a recompression shock travelling down the grid. Figure 4e shows a velocity vector map of the flow field. The vector lengths are scaled relative to the largest velocity magnitude in the flow field at that time. Any velocity vector whose magnitude is less than ten per cent of the largest magnitude is not plotted. Cratering caused by the expanding explosive products is well under way. The low-velocity toroidal center of the recompression region, centered at a radius of 2.8 cm, and a height of 20 cm, is also evident in Figure 4e.

The hydrocode solution reveals an interesting phenomenon associated with the development of the crater in the soil. The soil that was originally above the charge moves upward until it encounters the reflecting top boundary. It then rebounds back into the developing crater, but its travel is restricted by the high pressure explosive products. Meanwhile, the resistance of the surrounding soil restricts the radial expansion of the crater. These axial and radial constraints lead to the formation of an annular jet of soil, which apparently becomes the mechanism for ejecting the soil from the expanding crater. Figures 5a through 5e show a time-sequence of the annular soil jet development and corresponding crater growth. Those regions that show overlapping of contact surfaces are regions where mixing of soil, air, and explosive products occurs. The plots of the contact surfaces are constructed by connecting tracer particles that were placed along the original contact surfaces at time zero. While the tracer particles are fairly reliable in following the contact surfaces in the flow field regions away from the top boundary, there does seem to be some loss of definition of the contact surfaces near the top reflecting boundary, most likely due to the reflections off that top boundary. Figures 5a through 5e show, and analysis of the computation confirms, that there are large, continuous areas of soil contact on the top boundary, and hence the simulated target plate, at all times after the initial soil contact at 112 µs. Figures 5a through 5e also show the development of the reflected wave from the top boundary that travels back into the growing crater. The impact of the annular soil jet provides the bulk of the target plate loading after 130 µs. By 500 µs the soil jet's radial expansion has slowed considerably. During most of the time after 300 µs, the soil jet impacts the top boundary at a radius corresponding to the outer corners of the target plate. By 603 µs the soil jet has moved off the area covered by the 25.4 cm square plate, and the computation is halted at this time. At this time, it appears that the soil throughout the lower sections of the flow field has
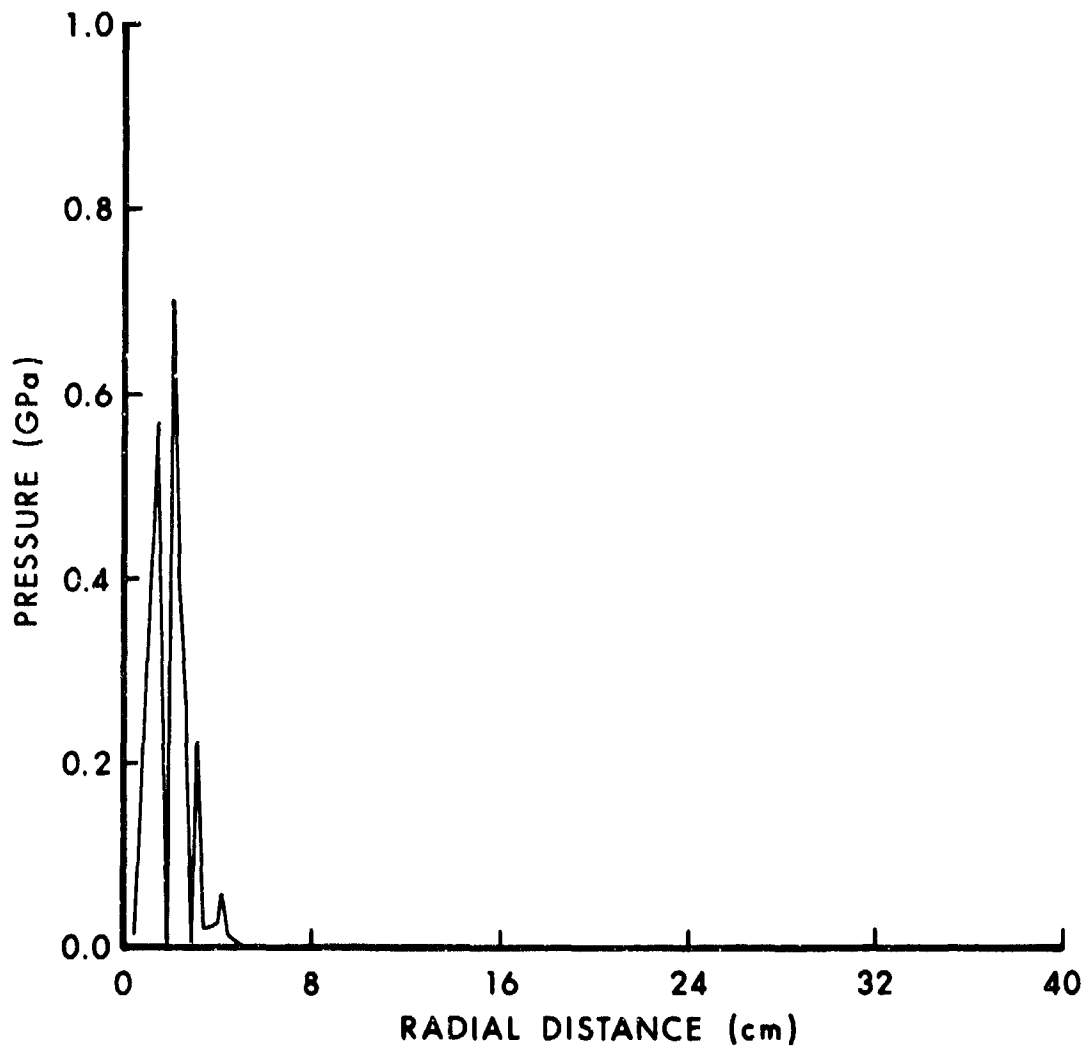
24

Figure 4c: The pressure along the
top boundary at 128 µs.
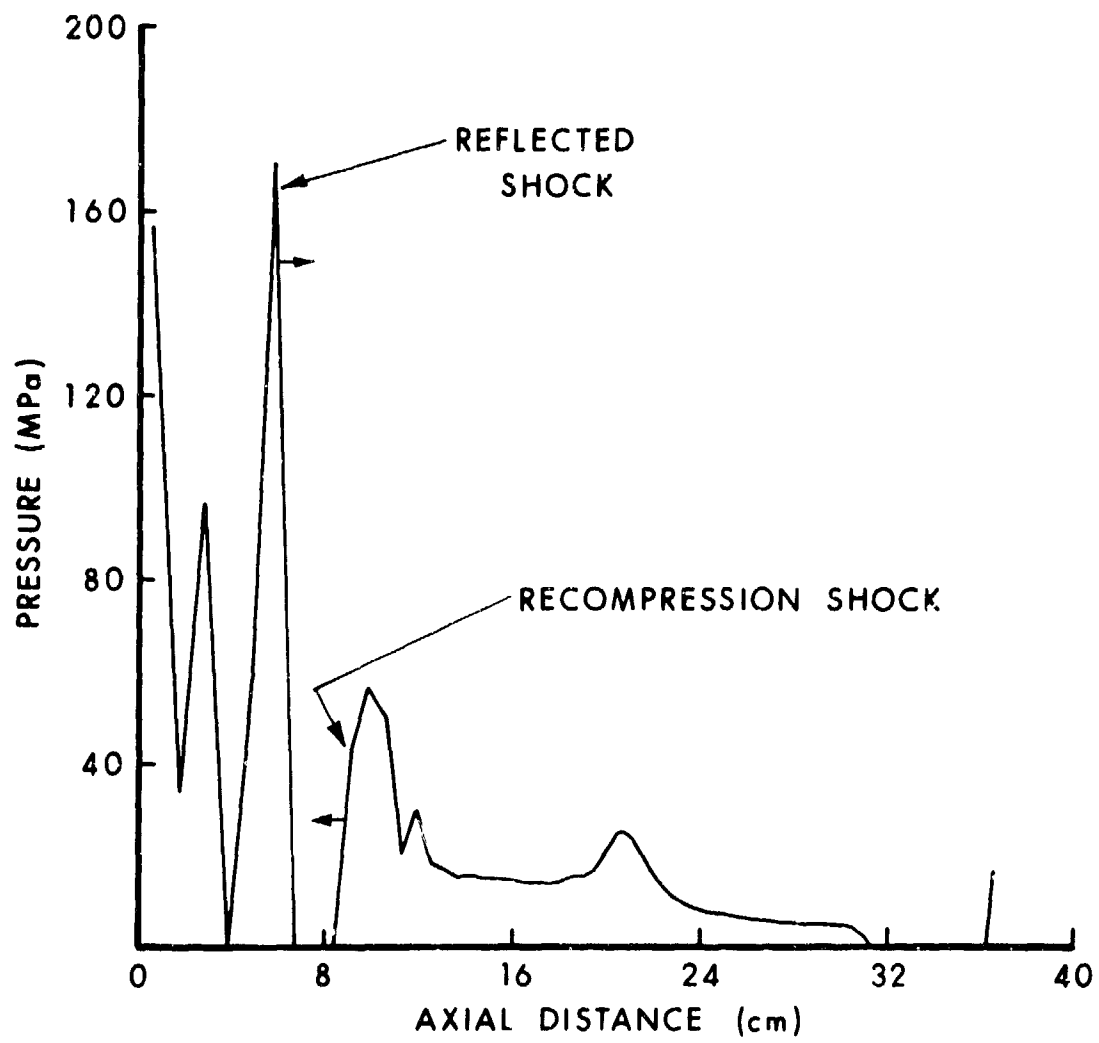
Figure 4d: Spatial cut of pressure, first column of
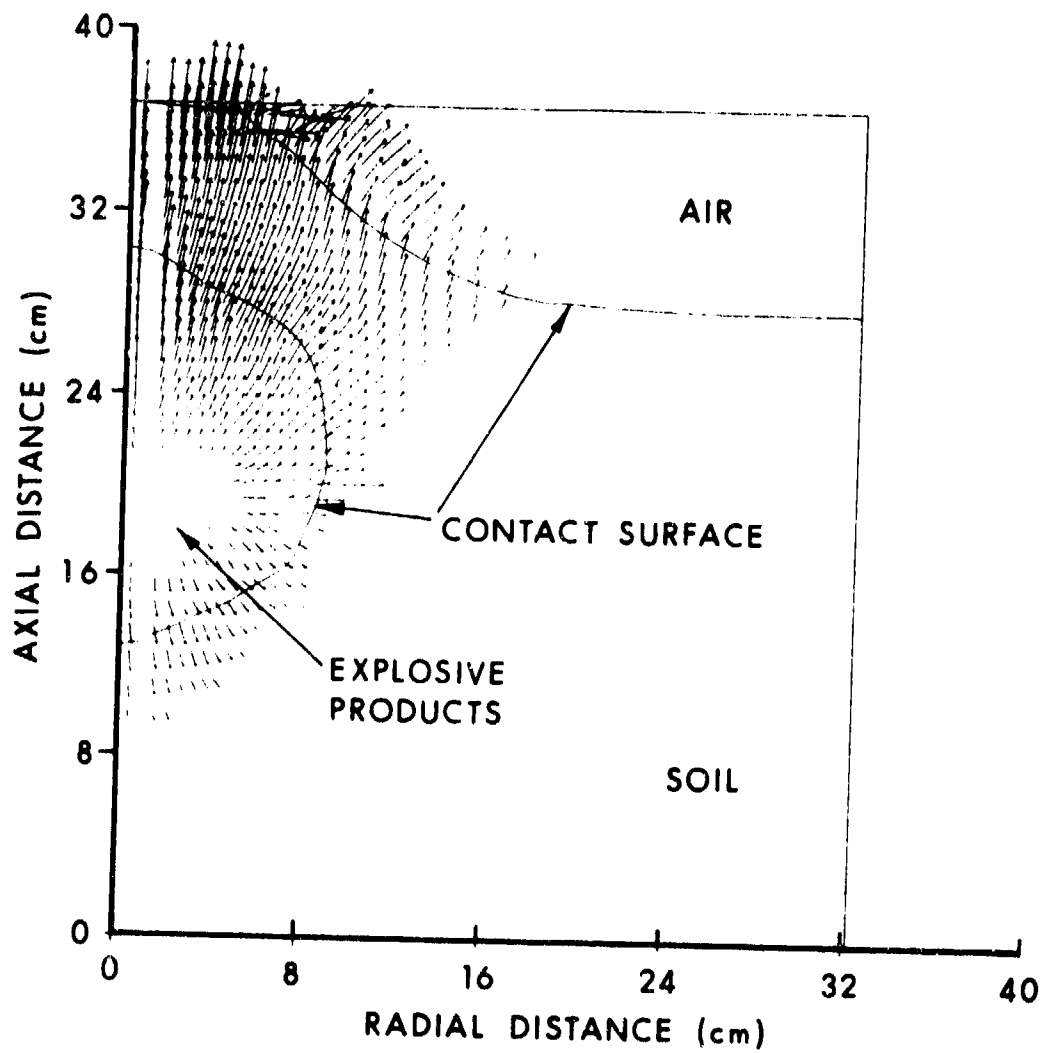cells along the axis of symmetry, 128 µs.

Figure 4e: The computational flow field at 128 µs.
Velocity vectors are plotted for every second
cell in the axial and radial directions.

27
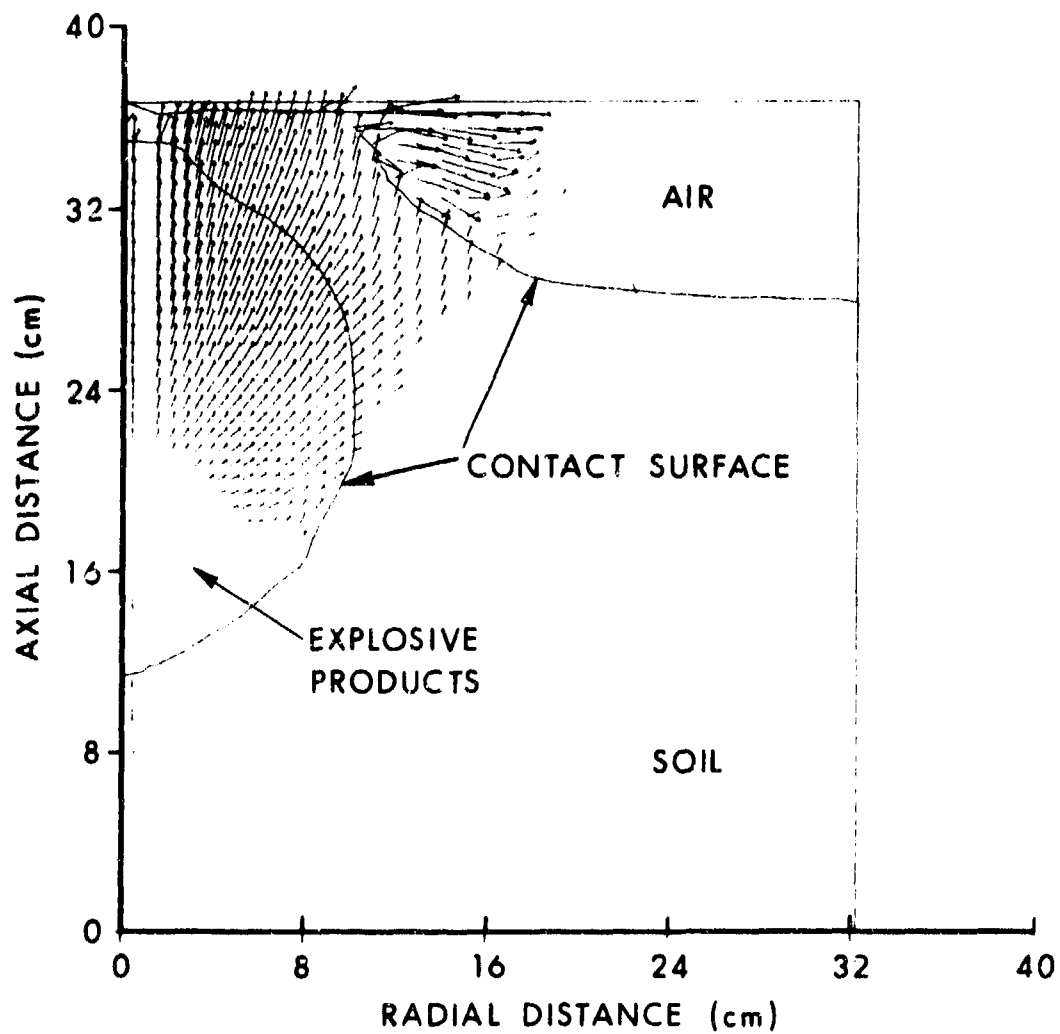
Figure 5a: The computational flow field at 205 μs; the soil is beginning to move out radially; an annular soil jet is beginning to develop. Velocity vectors are plotted for every second cell in the axial and radial directions.
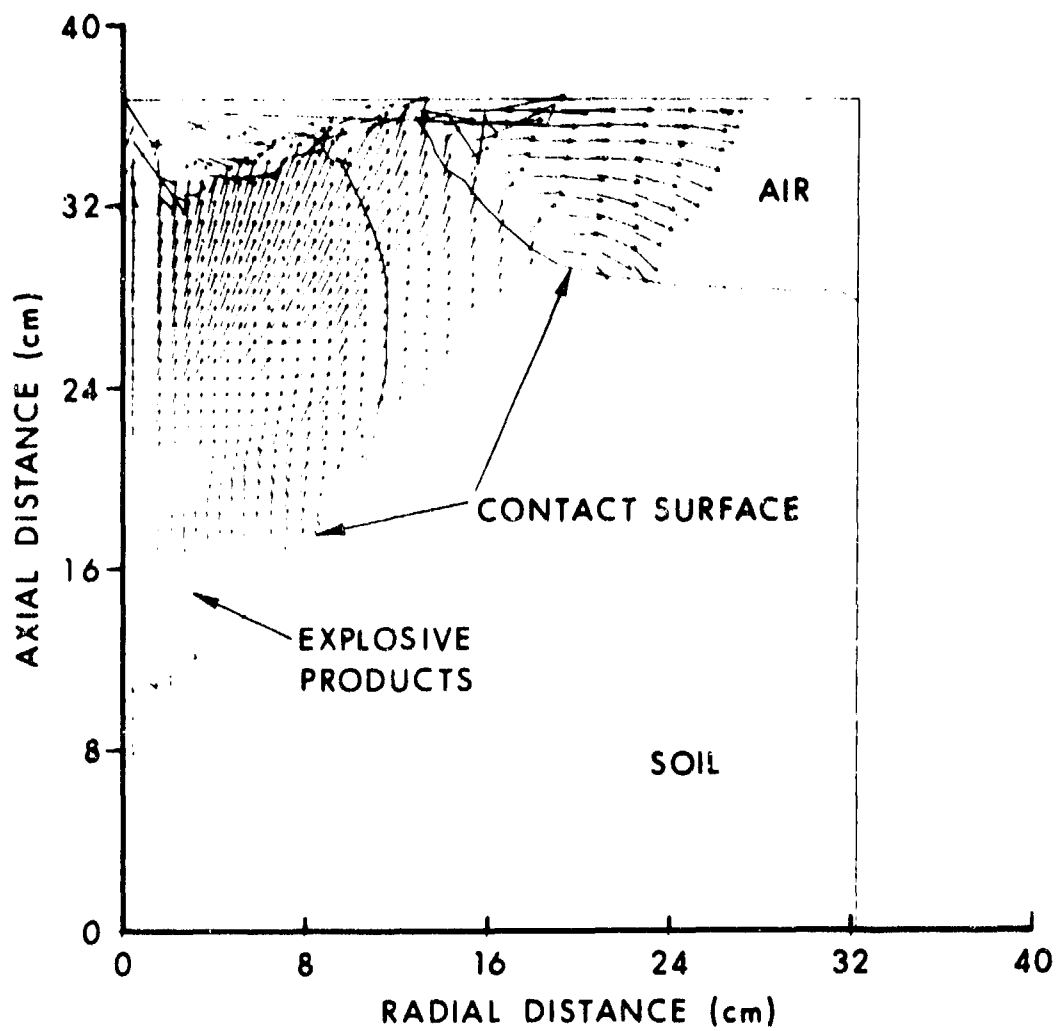
Figure 5b: The computational flow field at 301 μs, reflected wave
from top boundary developing, annular soil jet development
continuing. Velocity vectors are plotted for every
second cell in the axial and radial directions.

29
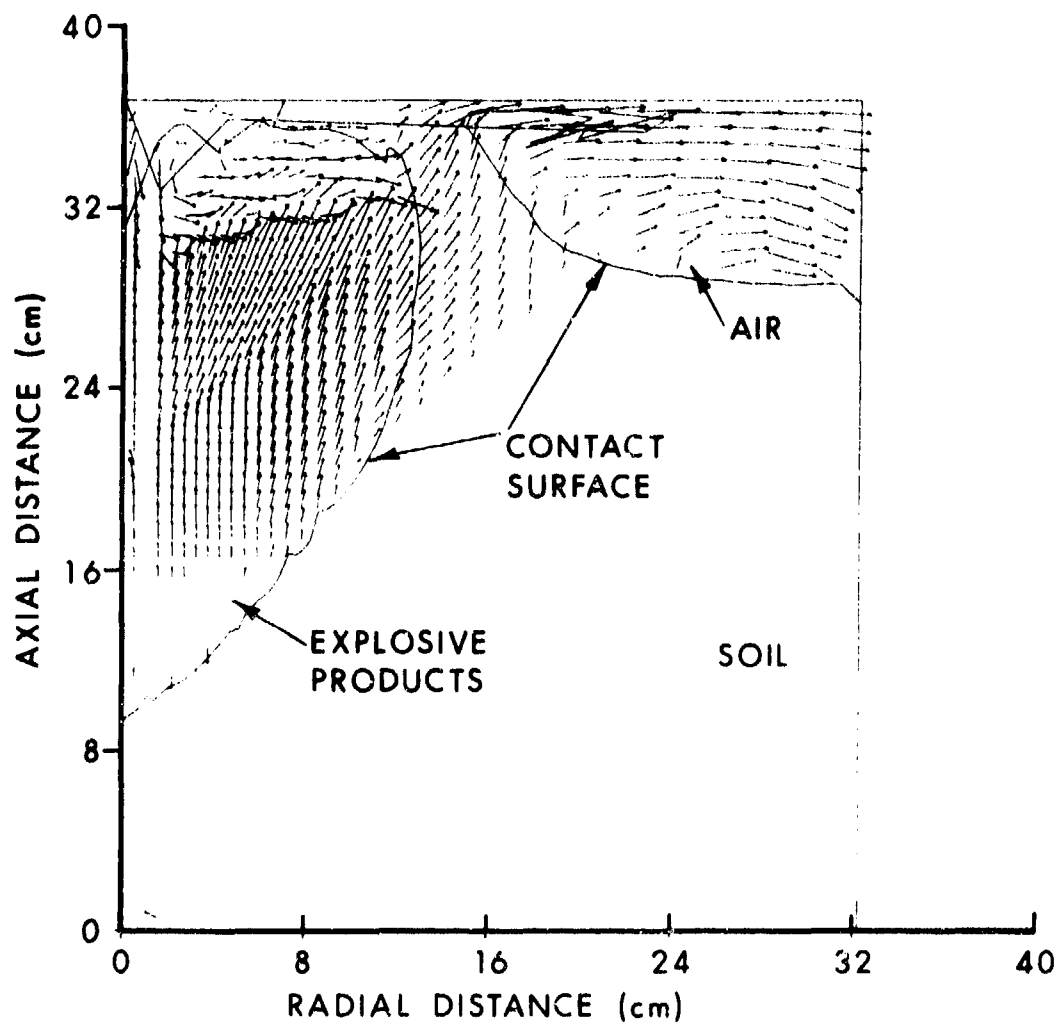
Figure 5c: The computational flow field at 398 μs, the reflected
wave from the top boundary and the annular soil jet fully
developed. Velocity vectors are plotted for every
second cell in the axial and radial directions.

30

Figure 5d: The computational flow field at 502 µs, the annular
soil jet persisting at 16 cm radius, the reflected wave from
the top boundary continuing to move into crater. Velocity
vectors are plotted for every second cell in the axial
and radial directions.

Figure 5e: The computational flow field at 603 μs, the annular
soil jet persisting near 16 cm radius, the reflected wave from
the top boundary still moving back into the crater.
Velocity vectors are plotted for every second cell
in the axial and radial directions.

32

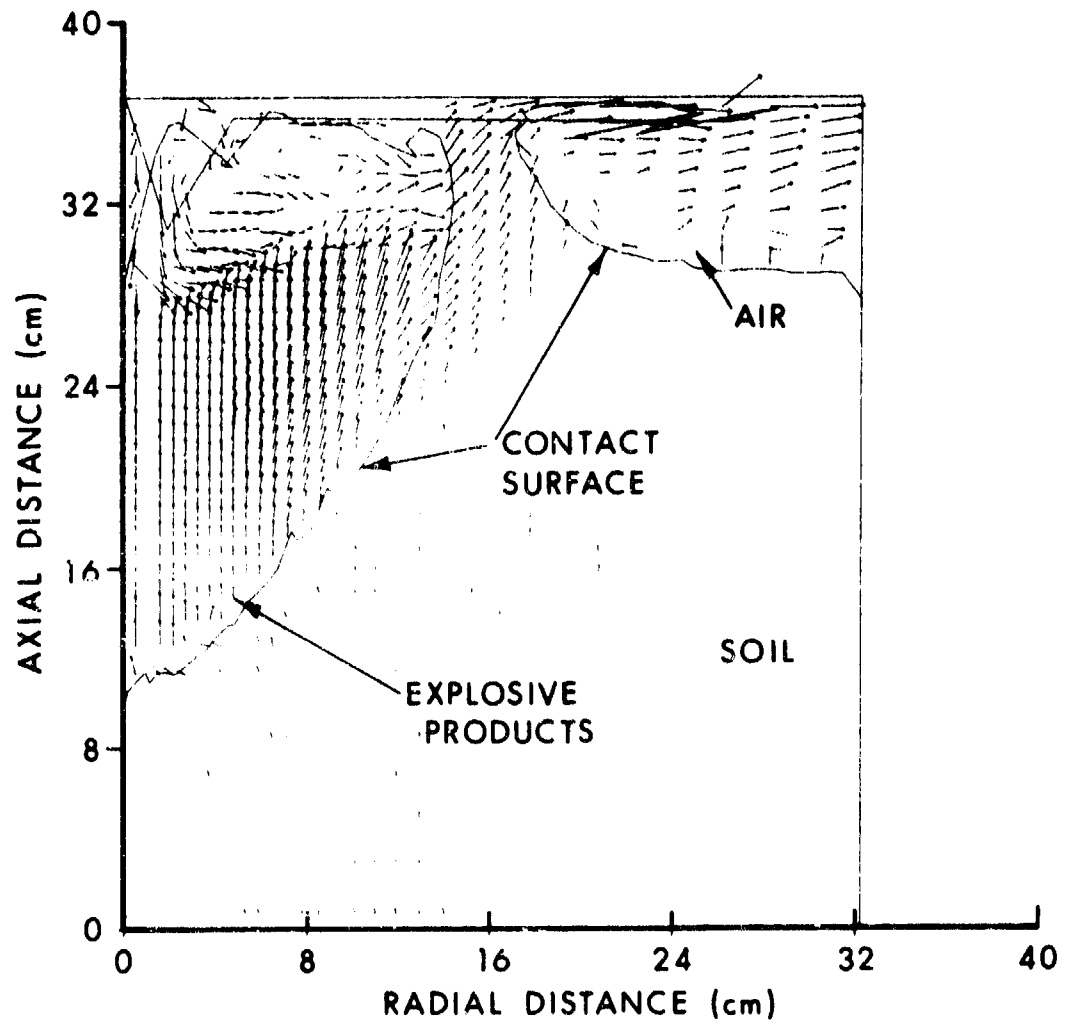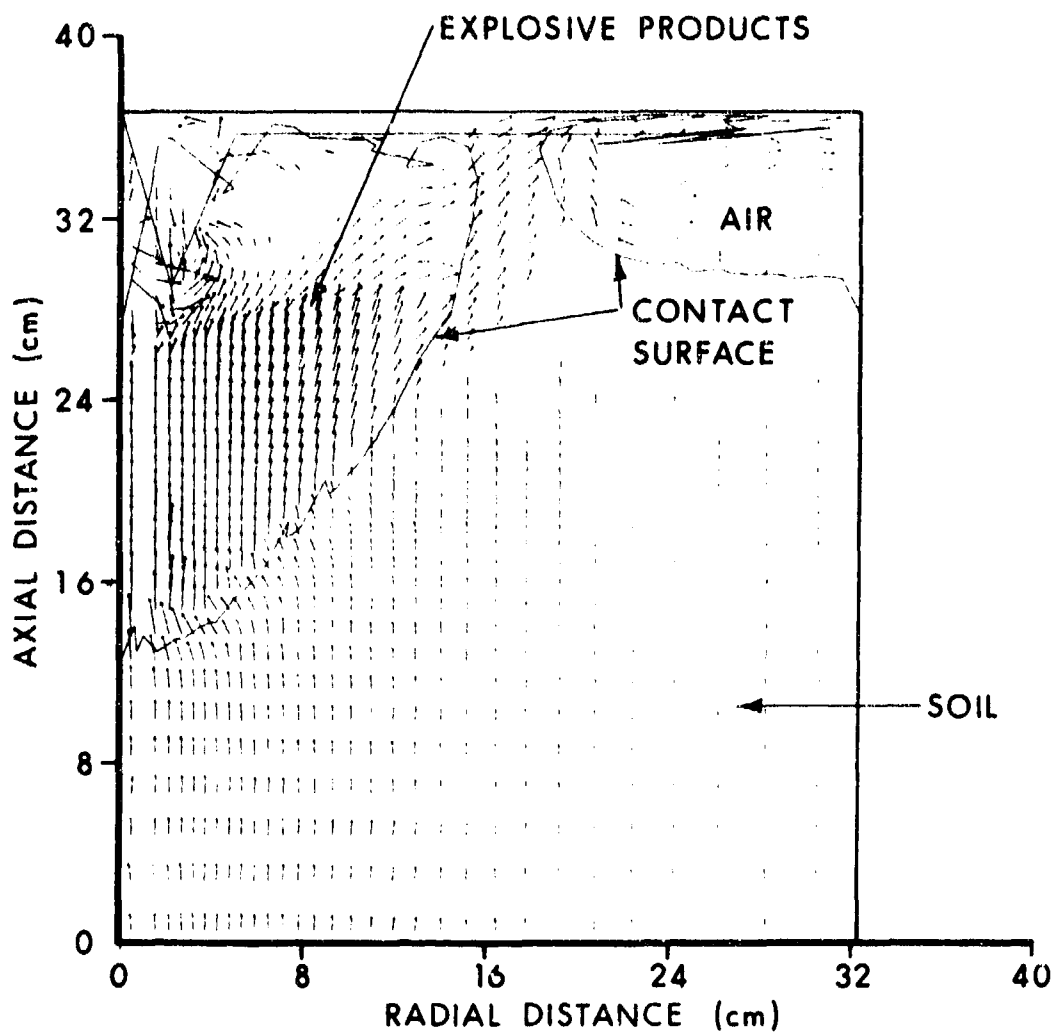begun a bulk upward movement. This is almost surely an artifact of the code, as will be discussed later. Figure 6 shows the pressure distribution on the top boundary of the computational flow field at 398 µs. The large pressure peak is due to the soil jet (see Figure 5c). This type of pressure distribution is typical for the time during which the soil jet exists.

As mentioned previously, the computation is carried out to 603 µs, real-time. The target plate is represented by a rigid, stationary, square plate, 25.4 cm on a side, centered above the mine. The total impulse, gage, on the target plate is computed by:

$$
\text{Total Impulse} = \sum_{j=1}^{j=J-1} \sum_{i=1}^{i=N} A_i \left(\frac{P_{i,j} + P_{i,j+1}}{2} - P_a \right) \left(t_{j+1} - t_j \right), \quad (5)
$$

where

J = the number of points in time at which loading data for the top boundary was stored on a data tape (loading data was stored every 5 computational cycles for this problem),

N = the number of flow field cells intersected by the target plate,

A_i = the area of the intersection of the ith flow field cell with the target plate (please see following discussion for details),

$P_{i,j}$ = the pressure in the ith flow field cell at the jth point in time,

P_a = the assumed, constant, atmospheric pressure behind the rigid, immobile target plate, and

t = the time.

Figure 7 shows a top view of the grid for the hydrodynamic flow field used in this DORF computation, with the axis of symmetry normal to the page and located at point 0. The square ABCD represents the square target plate, where each side is 25.4 cm. The concentric circles indicate the outer radial boundary of every fifth flow field cell in the radial, or I, direction. The grid spacing for the deformation computation (see Section V), 20 even cells per side of square AEOF, is also shown. The loading as computed by using Equation (5) includes that contribution from each flow field cell which intersects the square ABCD, proportional by the intersect of the flow field cell with the target plate.
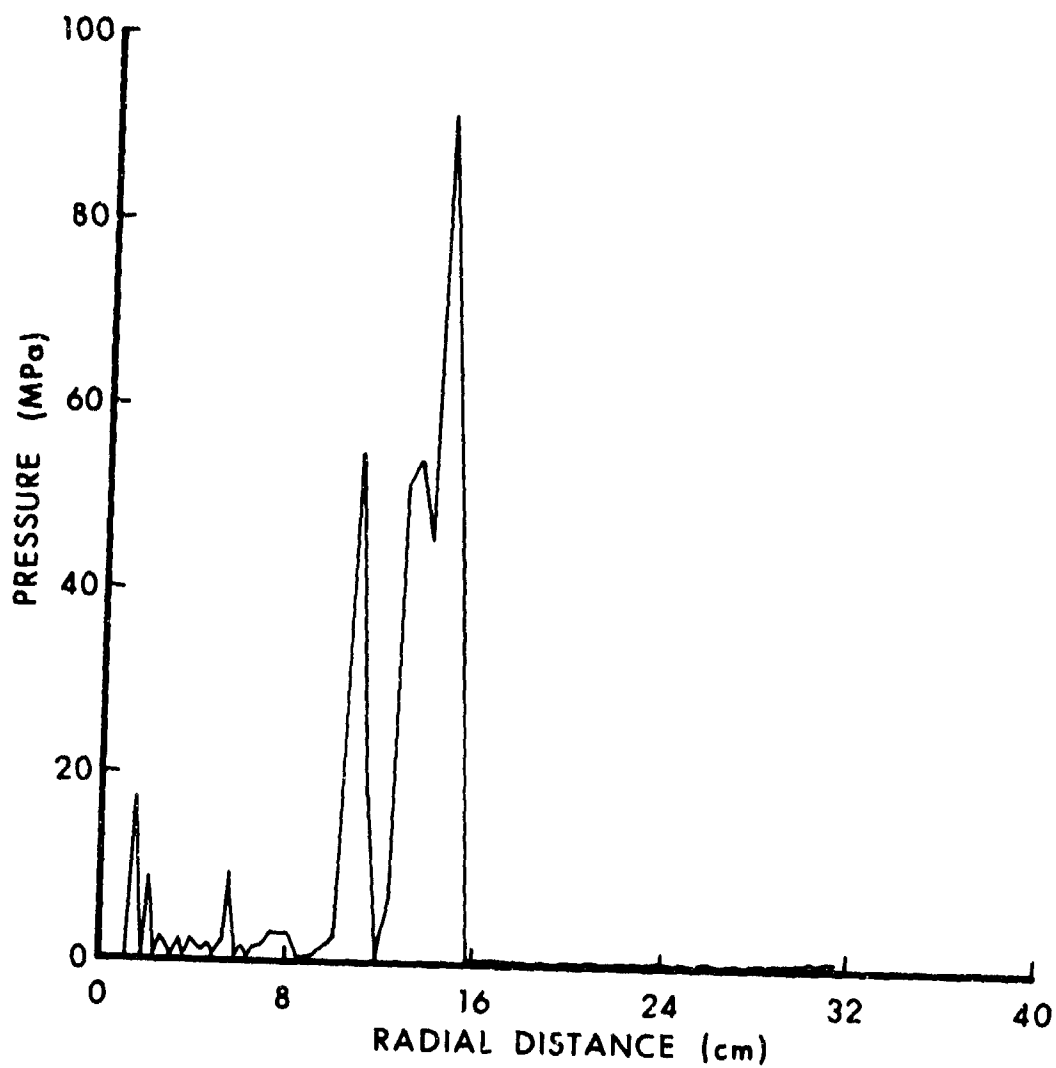
33

Figure 6. Pressure distribution on top boundary of computational flow field at 398 μs. High pressure peak due to soil jet impact.
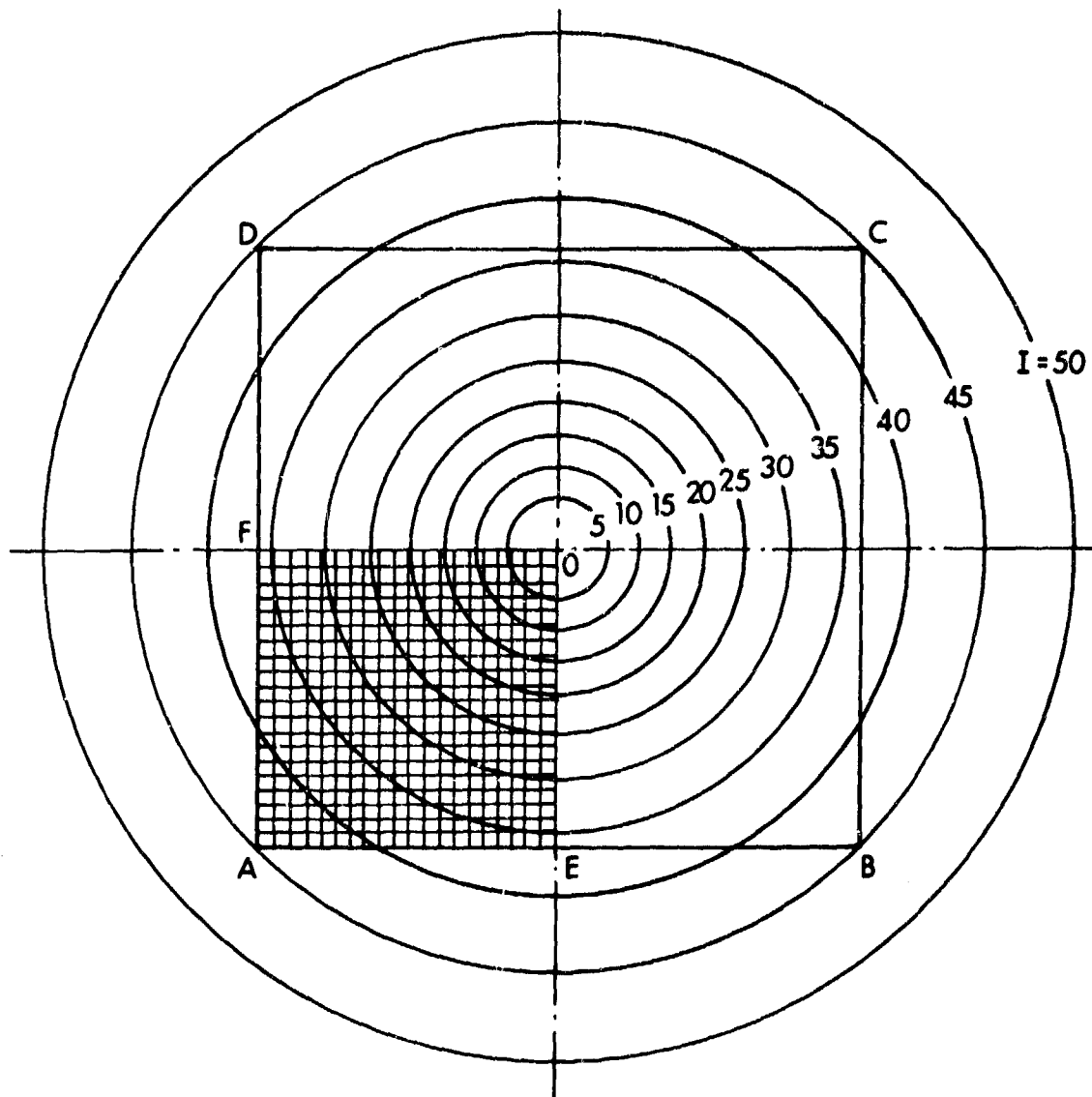
34

Figure 7. A top view of the intersection of the 25.4 cm
square target plate ABCD with the finite difference
grid for the DORF loading computation, and the
grid for the REPSIL response computation

As mentioned previously, the target is represented by a rigid stationary, square plate, 25.4 cm on a side, centered above the mine. Figure 8a shows a plot of total impulse, gage, versus time on the target plate. As may be seen in Figure 8a, the initial airblast makes an insignificant contribution to the total impulse. The subsequent total impulse is almost entirely due to the impact of the soil. The total impulse reaches an apparent plateau at 0.77 kN-s at 603 µs, 4.5% above that predicted by the correlation function generated by Westine and Hokanson[16]. The impulse correlation function by Westine and Hokanson[16] provides only total values for impulse, and not a time-history. Figure 8b is a plot of resultant force, gage, versus time on the target plate, computed by

$$\text{Force} = \sum_{i=1}^{i=N} A_i \ (P_i - P_a),\tag{6}$$

where

P_i is the pressure in the ith flow field cell,

and the other variables are as defined for Equation (5). The large, initial peak corresponds to the arrival of the soil at the target plate.

The DORF computer simulation also furnishes the time-history of the crater volume, as may be seen in Figure 9. The crater undergoes rapid, monotonic growth up until 325 µs, at which time the growth becomes somewhat erratic. The peak crater volume of 4.52×10^3 cm^3 occurs at 400 µs; by 603 µs it has fallen to 4.02×10^3 cm^3. This decrease in volume at later time is most likely an artifact of the code, possibly caused by the artificial reflection of the shock wave back into the soil at the bottom transmissive boundary. It appears that something, most likely the reflected wave mentioned above, is causing a bulk, upward movement of the soil. Figures 5a through 5e show the development of this upward movement. While this casts some doubt on the calculation of the late-time crater volume, it does not appear to have affected the target plate loading calculation. This is so because this artificial wave was detected during one of the several routine, intermediate analyses of the solution at a time shortly after its appearance at the bottom boundary as an apparent artificial reflection of the incident shock wave. The computation was stopped at 603 µs, when the leading edge of this wave was still several cells away from the top boundary, the area of primary interest in this computation.

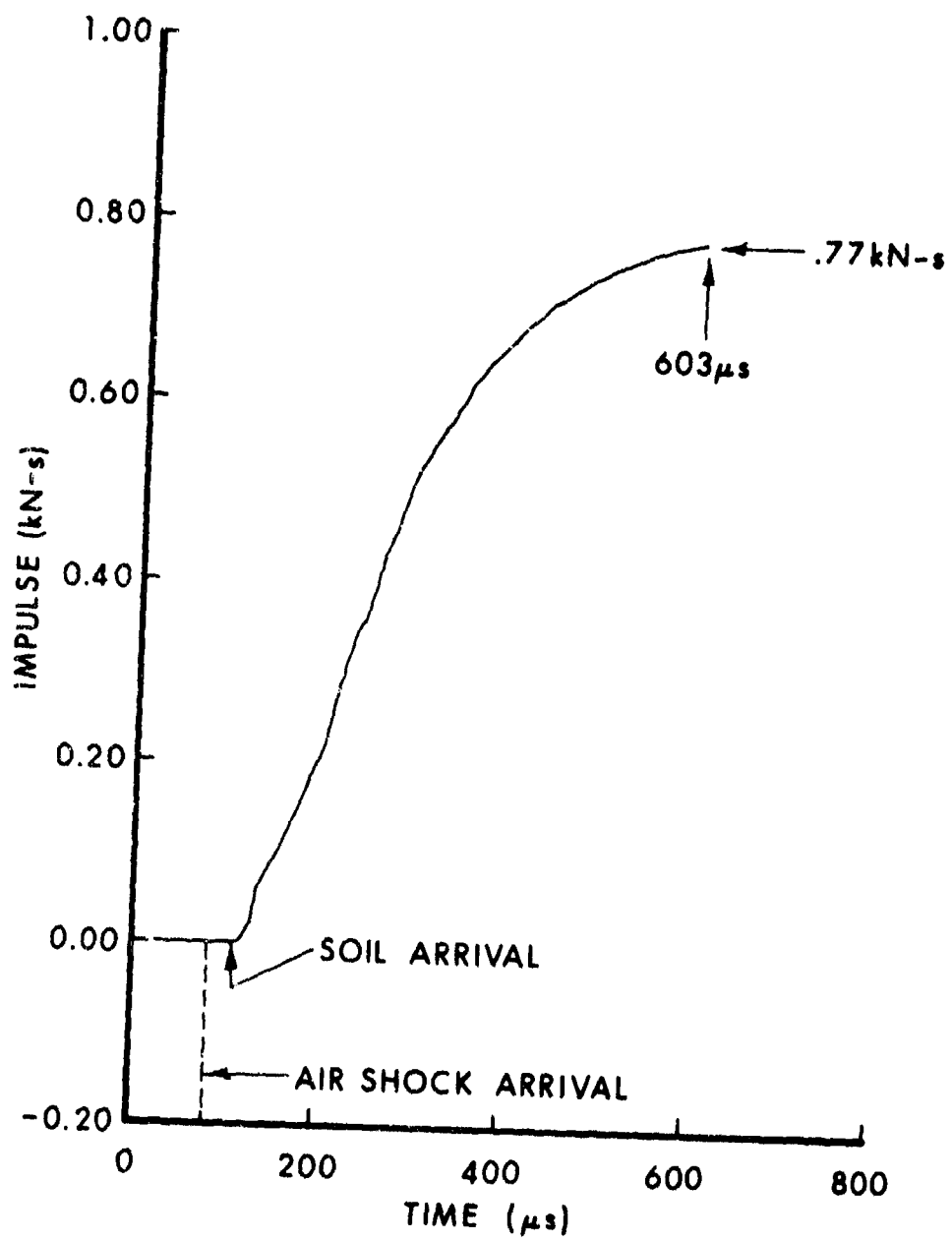36

Figure 8a: Impulse, gage, integrated over space and time on the 25.4 cm square target plate.
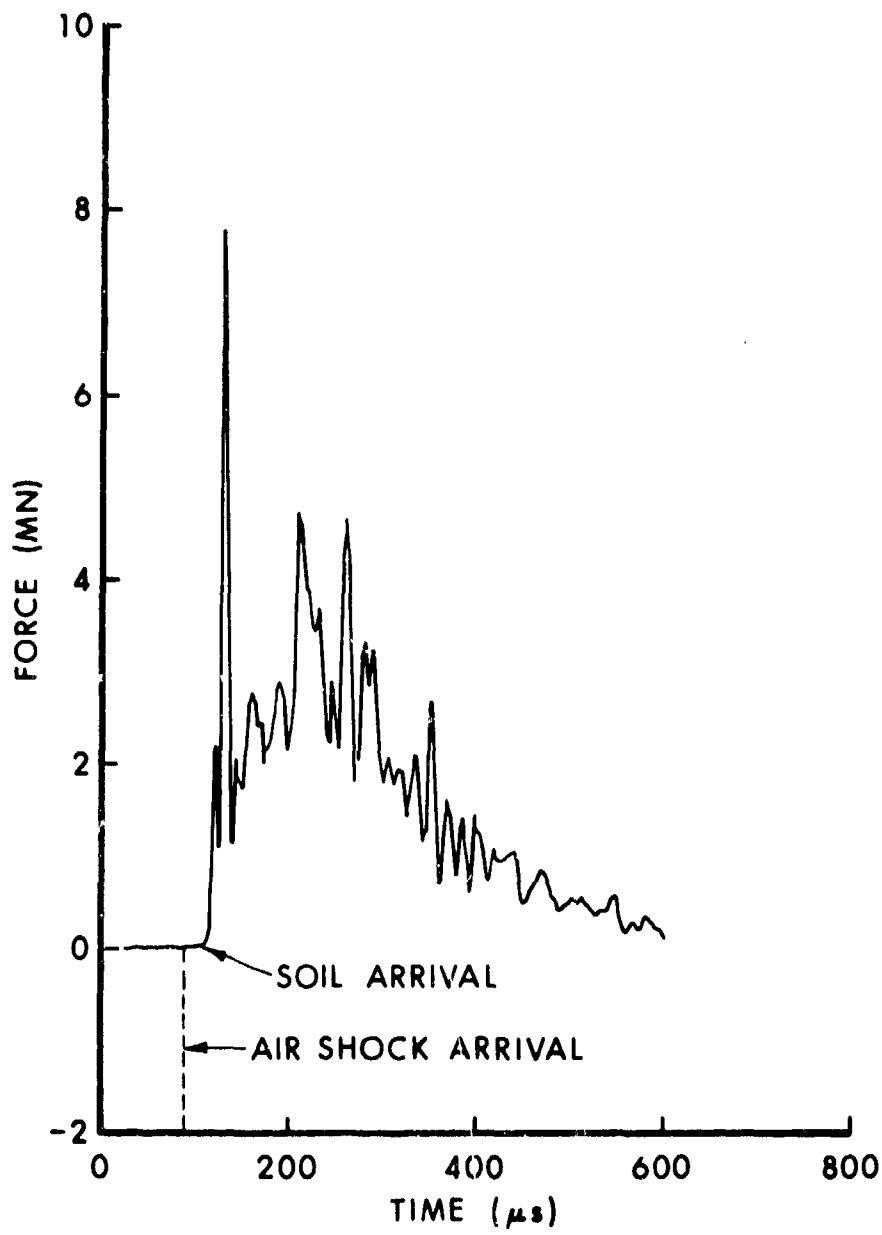
37

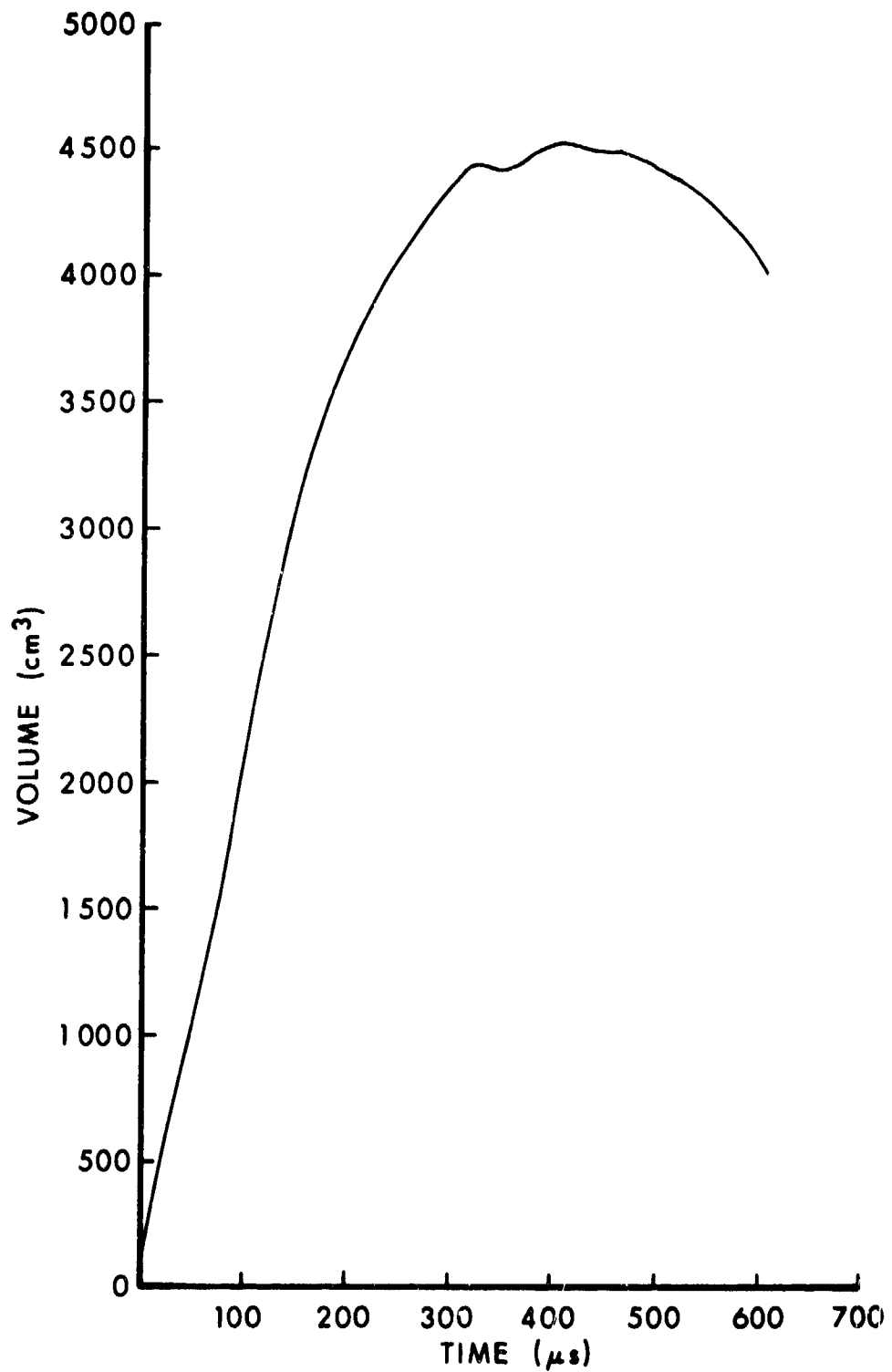Figure 8b: Resultant force; gage, on the 25.4 cm square target plate.

38

Figure 9:   Crater volume below original soil-air interface.

39

In a previous publication by Westine[22], and later in reports by Westine, Baker, and Wenzel[24] and Wenzel and Esparza[24], the volume for the crater made by a mine with no target above is predicted by the relation

$$V = 8.49 \ (W)^{0.681} \ (d)^{0.66}, \qquad (7)$$

for

$$\frac{W^{7/24}}{d} > 0.4$$

and

$$d > 0.0$$

Here, V represents volume in cubic feet, W represents charge weight in pounds, and d represents the depth of burial, in feet from the overburden surface to the top of the charge. Westine[22] indicates that the crater volume is relatively independent of the overburden material. For the case reported here, d is 0.188 feet and W is 0.583 lbm (therefore $W^{7/24}/d = 4.54 > 0.4$) and Equation (7) predicts a crater volume of 1.95 cubic feet, or $5.53 \times 10^4 \ cm^3$, 12.2 times greater than that predicted by the DORF computation reported here. The reason for this large discrepancy is not known, although it may be that Equation (7) is not applicable for small charges. The smallest charge weight apparently used to generate the correlation function is 116 kg of TNT. Westine[22] also presents a correlation for crater radius in the form of a plot, which, for the case presented here, predicts a crater radius ratio of $R/d = 8.32$. Because d is 5.74 cm, the predicted crater radius, assumed to be measured at the original ground level, is 47.7 cm. The corresponding crater radius predicted by the DORF calculation is 13.5 cm, so the crater radius predicted using Westine's correlation is 3.5 times that predicted by the DORF calculation, which is at least consistent with the volume discrepancy. Also, the crater radius and volume computed from the DORF solution are for the time 603 μs, the time at which the computation was stopped. At this time, the soil velocity in the annular soil jet was on the order of 230 m/s. It is

[22]Westine, P. S., Explosive Cratering, Journal of Terramechanics, Pergammon Press, 1970, Vol. 7, No. 2.

[23]Westine, P. S., Baker, W. F., and Wenzel, A. B., "Model Analysis of the Response of Armor Plate to Land Mine Attack," Technical Report No. 11255, US Army Tank Automotive Command, Warren, MI (February 1971).

[24]Wenzel, A. B., and Esparza, E. D., "Measurements of Pressures and Impulses at Close Distances from Explosive Charges Buried and in Air," SwRI Final Report on Contract No. DAAK02-71-C-0393 with MERDC, Fort Belvoir, VA., August 21, 1972.

assumed that crater growth would have continued beyond this time if it had not been necessary to stop the computation because of the strong artificial wave coming from the bottom boundary.

V. TARGET PLATE RESPONSE

The REPSIL[17] (Response of Elastic-Plastic Shells to Impulsive Loads) structural response program, selected to predict plate response to the buried land mine explosion, is capable of treating large transient deformations. The program accepts the loads generated by DORF on the target plate as a function of time and spatial coordinate. These features make REPSIL suitable for predicting plate response to a buried land mine explosion.

The computational model of the target plate takes advantage of the dual symmetry of the problem; only the lower left quarter of the target plate, as shown in Figure 10, is treated. Although the SwRI experimental boundary conditions did not achieve an ideally clamped edge condition, modeling them as such in REPSIL was the best available approximation to the experimental conditions. A 20 x 20 finite difference mesh is used in modeling one-quarter of the target plate.

The target plate material is reported[16] to be armor plate with a density of 7.833 Mg/m^3 and a yield strength of 789.45 MPa. Rolled homogeneous armor (RHA) was assumed for other material properties needed by REPSIL and are listed below:

Young's modulus	$E = 204.3$ GPa,
Poisson's ratio	$\nu = 0.3$,
Mass density	$\rho = 7.833$ Mg/m^3.

In the plastic range negligible error is introduced by assuming that RhA strain hardens independent of the strain rate[25]. This behavior is modeled in REPSIL by using a polygonal approximation to the uniaxial loading curve. The slope of the polygonal approximation for RHA changes at the following stress-strain points:

$$\sigma_1 = 789.45 \text{ MPa} \qquad \epsilon_1 = 0.004$$

$$\sigma_2 = 919.76 \text{ MPa} \qquad \epsilon_2 = 0.025$$

$$\sigma_3 = 962.58 \text{ MPa} \qquad \epsilon_3 = 0.075.$$

---

[25] Benck, R. F. and Robitaille, J. L., "Tensile Stress-Strain Curves--III, Rolled Homogeneous Armor at a Strain Rate of 0.42 s^{-1}," BRL-MR-2760, US Army Ballistic Research Laboratory, Aberdeen Proving Ground, MD (June 1977). (AD #A041560)
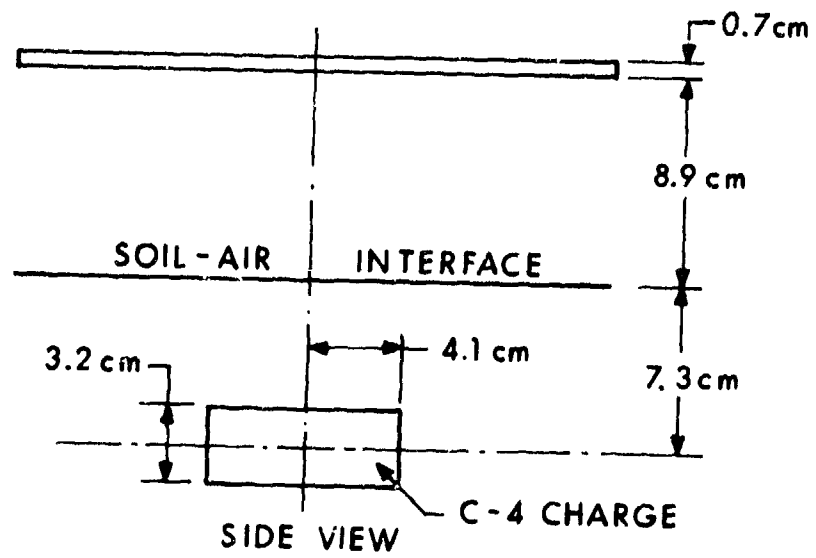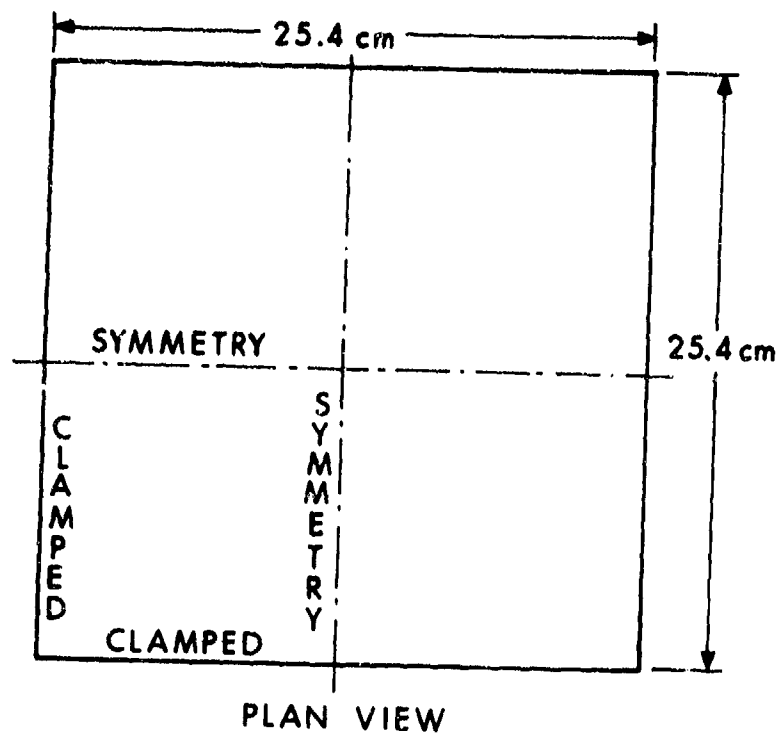
41

Figure 10. Geometry of armor target plate.

The dynamic loading of the rigid target plate determined by the DORF code provides the loading function P(r, t) for the structural response computations. These pressures are linearly interpolated in time and radius from the charge center to obtain the load at a given mesh point for each cycle of calculation in REPSIL (see Figure 7).

The deformation pattern of the target plate predicted by REPSIL is symmetric and free of any local denting, as can be seen in Figures 11 and 12, which show the target plate at 275 μs and 575 μs after detonation of the land mine. Local denting is not predicted due to the numerical approximation of the loading; pressure spikes narrower than one mesh spacing are not treated.

The jagged plate contour near the clamped edge in Figure 12 is due to the numerical modeling of a clamped edge. Near the clamped edge a one-sided differencing scheme is used to approximate derivatives. At the clamped boundary the components of the normal must remain fixed at their original values and hence the slope is also fixed at its original value of zero. Due to the one-sided difference formula for the first derivative used in REPSIL,

$$\frac{du_m^n}{dx} = 3 \ u_m^n - 4 \ u_{m+1}^n + u_{m+2}^n \qquad (8)$$

$$(u_m^n = 0 \text{ at the boundary}),$$

the normal component of displacement at one mesh spacing in from the clamped edge, u_{m+1}^n, is 1/4 the value of the corresponding normal component of displacement two mesh spacings in from the clamped edge, u_{m+2}^n, This, coupled with the central differencing to obtain first order derivatives away from the clamped edge, leads to the jagged edge condition near the clamped edge.

The initial soil impact with the target plate is indicated on Figure 13, which shows the total deflection history for the midpoint of the target plate. As anticipated, the maximum residual deformation occurs at the midpoint of the target plate. REPSIL calculates a maximum residual deflection of 5.59 cm when the target plate reaches its final equilibrium configuration (kinetic energy of plate is zero) as shown in Figure 13.

The amount of energy delivered to the target plate from a buried land mine explosion, based on the rigid body motion of a mechanical system having a single degree-of-freedom[16], is the square of the total impulse delivered by the explosive products and soil, divided by twice the plate mass: this compares well with the total energy in the system as computed by REPSIL. The total impulse delivered to the target plate as computed using the DORF hydrocode is 0.77 kN-s, yielding an energy of 86.47 kJ being delivered to the target plate. The total impulse delivered to the target plate using the empirical relationship developed
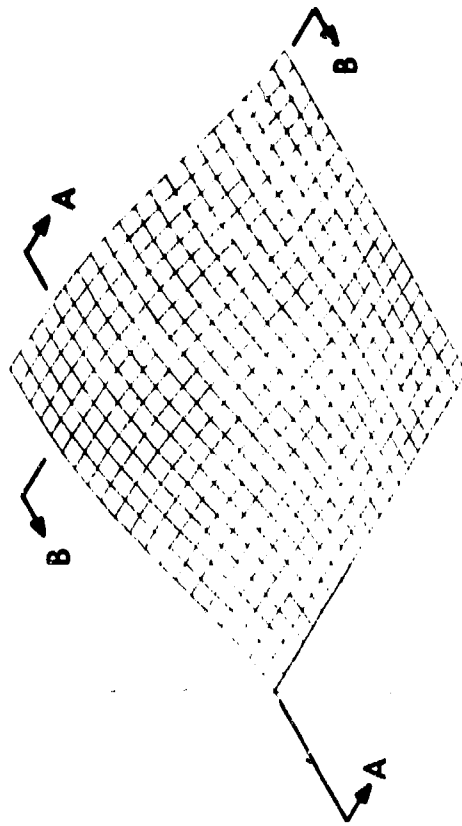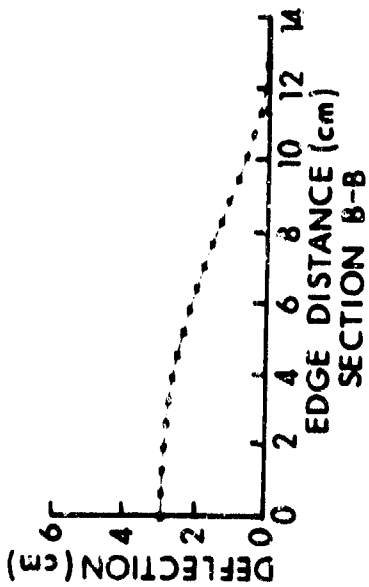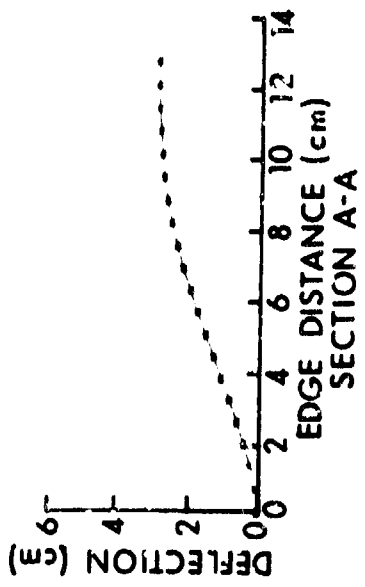
43

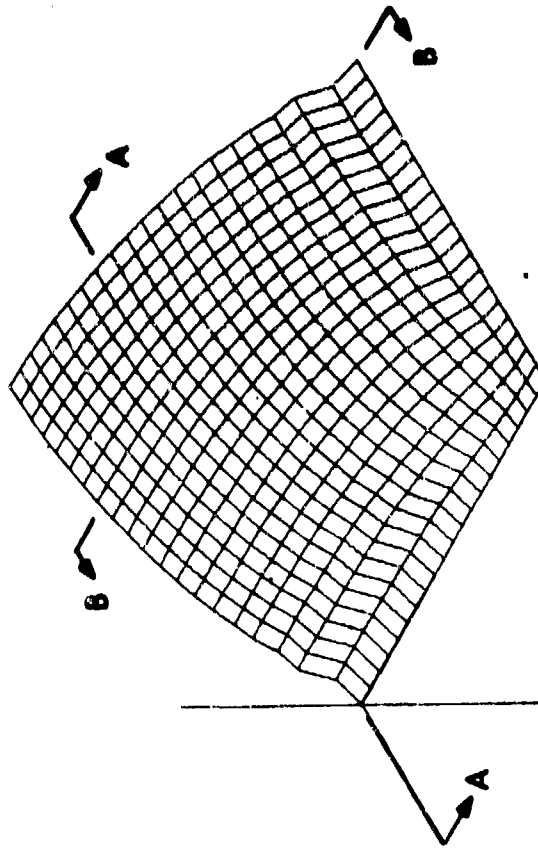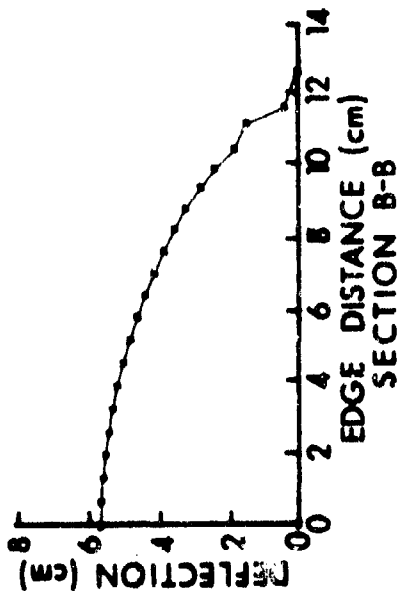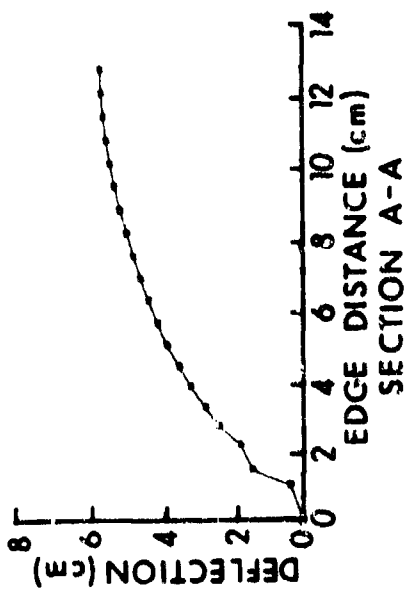Figure 11. Target plate deflection, time = 275 μs.
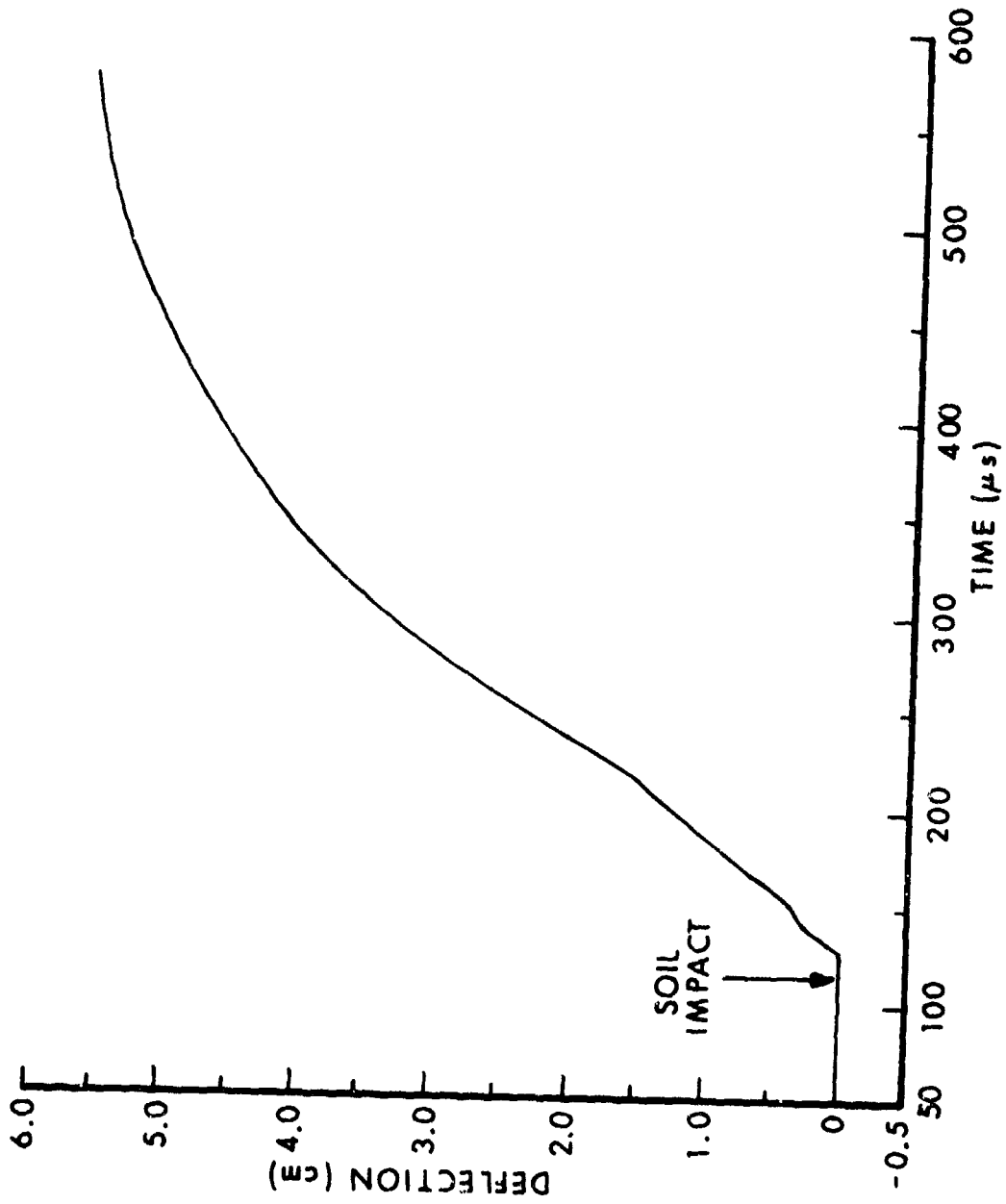
Figure 12. Target plate deflection, time = 575 µs.

45

Figure 15. Deflection time-history of the center of the target plate.

46

by Westine and Hokanson[16] is 0.741 kN-s, yielding an energy of 80.43 kJ.
The amount of energy delivered to the target plate, as computed by REPSIL,
is the external work done on each mesh integrated over the plate and is
represented by the external work curve (see Figure 14) which represents
the work done on the target plate by the external loads. The 88.41 kJ
computed by REPSIL compares well with the energy values computed above.
As can be seen in Figure 14, most of the energy delivered to the target
plate is dissipated in plastic deformation of the target plate, resulting
in a deformation profile that agrees well with predictions from empirical
relationships. In the SwRI experiments[16], a portion of the energy de-
livered to the target plate is dissipated in accelerating the target plate
and collar assembly.

Only the maximum residual deformation of the target plate is reported
in Reference 16 for test No. 36. However, a more detailed comparison of
the REPSIL predictions can be made by using the empirical expression
developed by Westine and Hokanson[16] for predicting the plate deformation
profile for a clamped-clamped flat plate centered over a buried land mine.
The expression provides a cubic fit to existing, experimentally observed,
deflection profiles for flat target plates subjected to a centered mine
blast and is restated below:

$$\frac{w}{W_0} = \left[1 - 0.42 \left(\frac{x}{X}\right)^2 - 0.58 \left(\frac{x}{X}\right)^3 \right] \left[1 - 0.42 \left(\frac{y}{Y}\right)^2 - 0.58 \left(\frac{y}{Y}\right)^3 \right] \qquad (9)$$

where,

W_0 is the maximum plate deflection,

w is the observed deflection at point (x, y),

x is the plate coordinate in X direction, measured from the
      charge center,

y is the plate coordinate in Y direction, measured from the
      charge center,

X is the half span of plate in X direction, and

Y is the half span of plate in Y direction.

Using Equation (9), a predicted deformation profile along either symmetry
plane of the quarter plate has been determined and is plotted in Figure
15; REPSIL's predicted plate deformation profile is also plotted. Both
curves are scaled to the maximum residual plate deformation of 5.131 cm
which was predicted by the Westine and Hokanson[16] procedure. The excel-
lent correlation between the curves illustrates that the Westine and
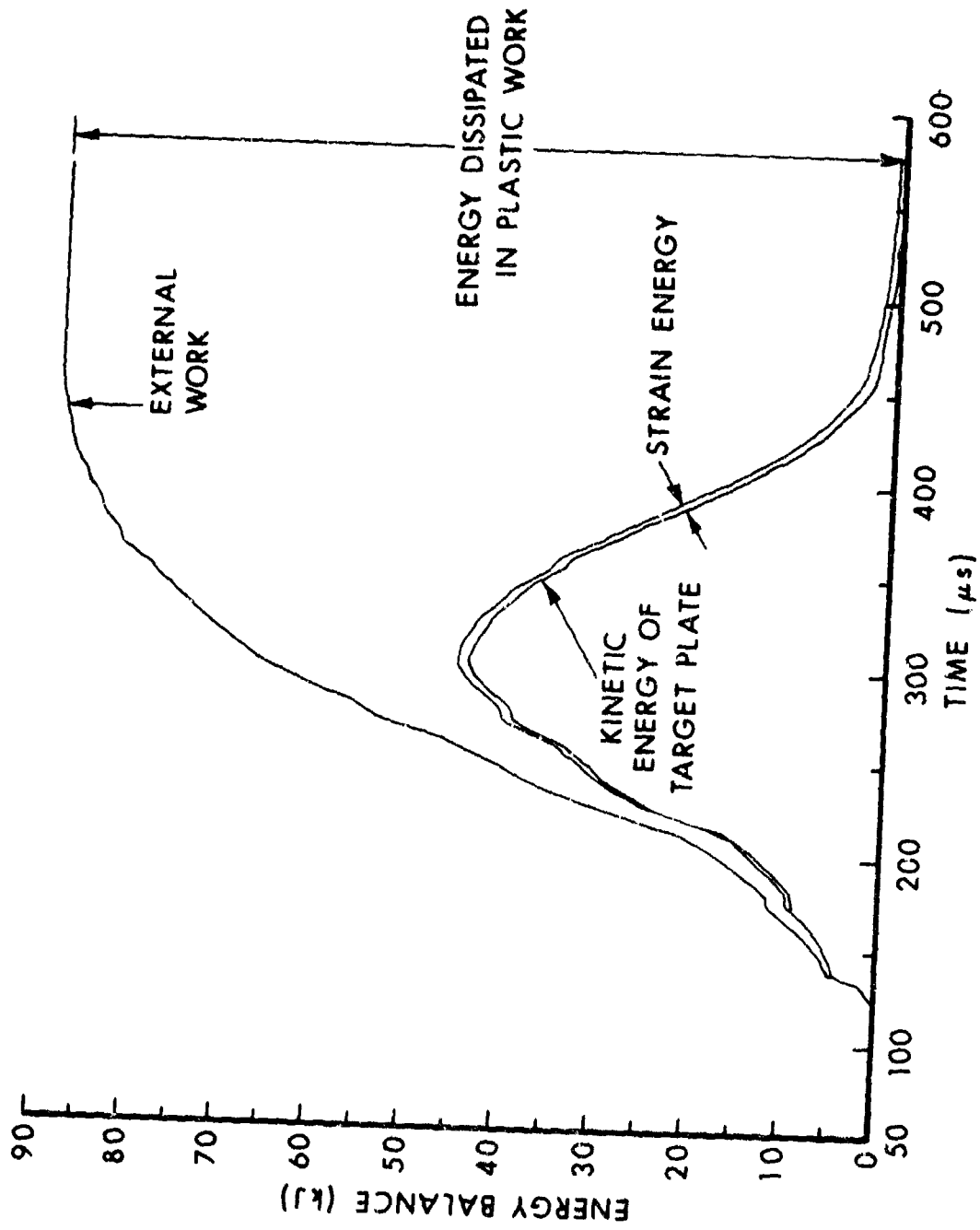Hokanson procedure provides a quick estimate for the maximum residual

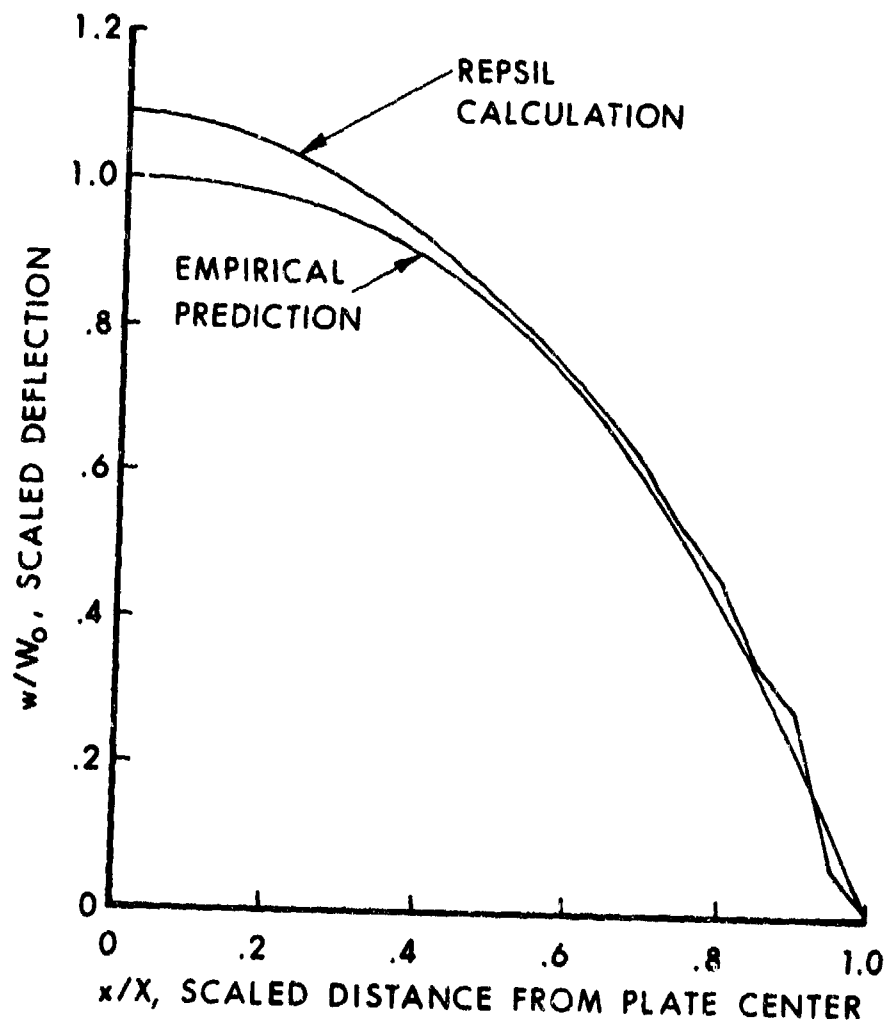Figure 14. Energy balance diagram for structural response of target plate.

48

Figure 15. Scaled target plate deformation
profile along either symmetry plane.

deformation and plate profile. However, by using the loading history for
the target plate generated by the DORF code as the loading function, the
REPSIL code provides a detailed analysis of the target plate, including
such items as both elastic and plastic strain predictions at predeter-
mined locations, target plate strain energy, and graphical representation
of the response.

From Figures 8a and 14 it can be seen that a portion of the impulse
is delivered to the target plate after the external work has leveled off.
This may cast some doubt on the assumption that the DORF calculations can
be uncoupled from the REPSIL calculations. This can be resolved by ob-
serving in Figure 8b that the resultant force on the target plate decays
rather rapidly, which allows for little plate deformation to occur even
though contributions are being made to the impulse.

VI. SUMMARY

The numerical simulation, reported here, of a field experiment[16]
performed and reported by SwRI has been compared with empirical correla-
tion functions[16]. The DORF hydrocode solution for the total impulse
delivered to the rolled homogeneous armor target plate is 4.5% above
that computed using the SwRI correlation function for impulse. The maxi-
mum residual deformation profile of the target plate, predicted by the
REPSIL structural response program, agrees to within 10% of the profile
computed using the SwRI correlation function. The DORF hydrocode and the
REPSIL structural response code give a reasonable estimate for the plate
deflection, even though the loading and response calculations are un-
coupled.

VII. RECOMMENDATIONS

Although the above stated comparisons of computed results versus
the empirical correlation functions show excellent agreement, there is
considerable room for improvement in both the DORF code and in the tech-
niques used here. The more significant recommendations for improvement
and for additional efforts are as listed below.

A. Add an accurate explosive detonation routine to the version of
DORF used here.

B. Add an appropriate equation of state to DORF to model the explo-
sive products.

C. Improve the DORF code's ability to model soil and investigate
the apparent crater volume and radius discrepancy.

D. Improve the numerical formulation of the transmissive boundaries
in DORF, with particular attention to the formulation of the bottom boun-
dary.

50

E. Modify the differencing technique in DORF to eliminate the errors caused by DORF's equal weighing of unequal cell volumes.

F. Establish a more detailed understanding of the artificial viscosity option in DORF. It was not used in this computation because it seems to have a significant effect on the solution beyond simply improving numerical stability, which is the all too generally accepted reason for its use.

G. Develop a clamped boundary model for REPSIL which allows plate slippage.

H. Couple a hydrodynamic code to compute loading with a structural response code suitable for computing plate response.

REFERENCES

1. Hanna, J. W., "An Effectiveness Evaluation of Several Types of Anti-Tank Mines," BRL-MR-616, US Army Ballistic Research Laboratory, Aberdeen Proving Ground, MD (June 1952). (AD #377342)

2. Bailey, R. A., Born, D., and Sultanoff, M., "Analysis of the Performance of the Mock-Up Booster Assembly for the Multi-Jet, Shaped Charge, Anti-Tank Mine," BRL-MR-584, US Army Ballistic Research Laboratory, Aberdeen Proving Ground, MD (October 1951). (AD #377333)

3. Haskell, D. F. and Reisinger, M. J., "Armored Vehicle Vulnerability Analysis Model - First Version, Introduction," BRL-R-1857, US Army Ballistic Research Laboratory, Aberdeen Proving Ground, MD (February 1976). (AD #B009638L)

4. Clark, E. L., "Testing of Anti-Armor Devices," BRL-CR-221, US Army Ballistic Research Laboratory, Aberdeen Proving Ground, MD (April 1975). (AD #B003825L)

5. Norman, R. M., "An Estimate of the Performance of the FRG Pandora Anti-Tank Mine" (U), BRL-MR-1754, US Army Ballistic Research Laboratory, Aberdeen Proving Ground, MD (July 1966) (SECRET-NOFORN). (AD #376685)

6. Cioffi, A. R. and Vincent, A. R., "Preliminary Estimates of the Vulnerability of Light Weight Armored Vehicles to Attack by Anti-Tank Mines" (U), BRL-TN-1197, US Army Ballistic Research Laboratory, Aberdeen Proving Ground, MD (June 1958) (CONFIDENTIAL). (AD #378697)

7. Norman, R. M., "An Estimate of the Performance of the XM34 Anti-Tank Mine" (U), BRL-MR-1774, US Army Ballistic Research Laboratory, Aberdeen Proving Ground, MD (August 1966) (CONFIDENTIAL).(AD #377250)

8. Norman, R. M. and Beichler, G. P., "Effectiveness Studies of the XM34 AT Mine" (U), BRL-TN-1640, US Army Ballistic Research Laboratory, Aberdeen Proving Ground, MD (December 1966) (CONFIDENTIAL).(AD #379091)

9. Norman, R. M. and Beichler, G. P., "An Estimate of the Performance of Buried XM34 Antitank Mines" (U), BRL-TN-1641, US Army Ballistic Research Laboratory, Aberdeen Proving Ground, MD (December 1966) (CONFIDENTIAL). (AD #379839)

10. Norman, R. M., "Deformation in Flat Plates Exposed to HE Mine Blast," AMSAA-TM-74, US Army Materiel Systems Analysis Agency, Aberdeen Proving Ground, MD (May 1970).

11. Haskell, D. F., "Deformation and Fracture of Tank Bottom Hull Plates Subjected to Mine Blast," BRL-R-1587, US Army Ballistic Research Laboratory, Aberdeen Proving Ground, MD (May 1972). (AD #901628L)

REFERENCES (Continued)

12. Johnson, Wallace E., "Code Correlation Study," AFWL-TR-70-144, Air
    Force Weapons Laboratory, Kirtland Air Force Base, NM (April 1971).

13. Miller, James E., "Preliminary Study of Target Load Prediction by
    Use of a Hydrodynamic Computer Code," BRL MR-2472, US Army Ballistic
    Research Laboratory, Aberdeen Proving Ground, MD (April 1975).
    (AD #B003829L)

14. Allison, W. Donald, private communication of as yet unpublished data.

15. Taylor, Geoffrey I., Sir, The Dynamics of the Combustion Products
    behind Plane and Spherical Detonation Fronts in Explosives, Pro-
    ceedings of the Royal Society of London, Series A, Vol. 200,
    22 February 1950.

16. Westine, Peter S. and Hokanson, James C., "Procedures to Predict
    Plate Deformations from Land Mine Explosions" (U), TACOM Technical
    Report No. 12049, US Army Tank Automotive Command, Warren, MI
    (August 1975) (CONFIDENTIAL).

17. Santiago, J. M., Wisniewski, H. L., and Huffington, N. J., Jr., "A
    User's Manual for the REPSIL Code," BRL Report 1744, US Army Ballistic
    Research Laboratory, Aberdeen Proving Ground, MD (October 1974).
    (AD #A003176)

18. Tillotson, J. H., "Metallic Equations of State for Hypervelocity
    Impact," GA-3216, General Atomic, Division of General Dynamics,
    San Diego, CA (July 1962).

19. Hill, L. R. and Johnson, W. E., "Energy Partitioning during Hyper-
    velocity Impact on Rocks," SC-R-70-4402, Sandia Laboratories,
    Albuquerque, NM (December 1970).

20. Allen, R. T., "Equation of State of Rocks and Minerals," GAMD 7834,
    General Atomic, Division of General Dynamics, San Diego, CA (March
    1967).

21. Johnson, W. E., private communication (November 1974).

22. Westine, P. S., Explosive Cratering, Journal of Terramechanics,
    Pergammon Press, 1970, Vol. 7, No. 2.

23. Westine, P. S., Baker, W. E., and Wenzel, A. B., "Model Analysis of
    the Response of Armor Plate to Land Mine Attack," Technical Report
    No. 11235, US Army Tank Automotive Command, Warren, MI (February
    1971).

24. Wenzel, A. B., and Esparza, E. D., "Measurements of Pressures and
    Impulses at Close Distances from Explosive Charges Buried and in
    Air," SwRI Final Report on Contract No. DAAK02-71-C-0393 with MERDC,
    Fort Belvoir, VA., August 21, 1972.

REFERENCES (Continued)

25. Benck, R. F. and Robitaille, J. L., "Tensile Stress-Strain Curves--
    III, Rolled Homogeneous Armor at a Strain Rate of 0.42 s⁻¹,"
    BRL-MR-2760, US Army Ballistic Research Laboratory, Aberdeen Proving
    Ground, MD (June 1977). (AD #A041560)

DISTRIBUTION LIST

No. of Copies	Organization
12	Commander Defense Documentation Center ATTN: DDC-TCA Cameron Station Alexandria, Virginia 22314
1	Director of Defense Research and Engineering ATTN: Dir/Tech Info Washington, D.C. 20301
1	Director Defense Advanced Research Projects Agency 1400 Wilson Boulevard Arlington, Virginia 22209
1	Director Weapons Systems Evaluation Group, ODDR&D ATTN: CPT Donald E. McCoy 400 Army-Navy Drive Washington, DC 20305
1	Assistant Secretary of Defense (I&L) Washington, DC 20310
1	Staff Specialist for Materials and Structures ATTN: Mr. J. Persh Office of Deptuy Under Secretary of Defense for Research and Engineering (ET) Room 3D1089, The Pentagon Washington, DC 20301
1	Director Defense Communications Agency ATTN: NMCSSC (Code 510) Washington, DC 20305
2	Director Defense Intelligence Agency ATTN: DT-1C, Dr. J. Vorona DT-2 Washington, DC 20301

No. of Copies	Organization
3	Director Institute for Defense Analyses ATTN: Dr. J. Menkes Dr. J. Bengston Tech Info Ofc 400 Army-Navy Drive Arlington, Virginia 22202
1	Commander US Army Materiel Development and Readiness Command ATTN: DRCDMA-ST 5001 Eisenhower Avenue Alexandria, Virginia 22333
1	Director DARCOM, ITC ATTN: Dr. Chiang Red River Depot Texarkana, Texas 75501
1	Commander US Army Aviation R&D Command ATTN: DRSAV-E 12th and Spruce Streets St. Louis, MO 63166
1	Director US Army Air Mobility Research and Development Laboratory Ames Research Center Moffett Field, CA 94035
1	Commander US Army Electronics Command ATTN: DRSEL-RD Fort Monmouth, NJ 07703
1	Commander US Army Missile Research and and Development Command ATTN: DRDMI-R Redstone Arsenal, AL 35809

DISTRIBUTION LIST

No. of Copies	Organization	No. of Copies	Organization
1	Commander US Army Tank Automotive Research and Development Cmd ATTN: DRDTA-RHEL, Mr. M. Hennessey Warren, Michigan 48090	2	Commander US Army Armament Research & Development Command ATTN: DRDAR-LCM-SP STINFO, DRDAR-TSS Dover, New Jersey 07801
2	Commander US Army Tank Automotive Research and Development Cmd ATTN: DRDTA DRDTA-RWL Warren, Michigan 48090	1	Commander US Army Harry Diamond Labs ATTN: DRXDO-TI 2800 Powder Mill Road Adelphi, MD 20783
2	Commander US Army Mobility Equipment Research & Development Command ATTN: Tech Docu Cen, Bldg. 315 DRSME-RZT Fort Belvoir, Virginia 22060	3	Commander US Army Materials and Mechanics Research Center ATTN: DRXMR-ATL DRXRD, Dr. S. C. Chou DRXMR-TS, Dr. J.Adachi Watertown, MA 02172
1	Commander US Army Mobility Equipment Research & Development Command ATTN: Mr. J. Montgomery Fort Belvoir, Virginia 22060	1	Commander US Army Natick Research and Development Command ATTN: DRXRE, Dr. D. Sieling Natick, MA 01762
1	Commander US Army Armament Materiel Readiness Command ATTN: DRSAR-LEP-L Rock Island Illinois 61202	1	Commander US Army Foreign Science and Technology Center ATTN: Rsch & Data Branch Federal Office Building 220 7th Street, NE Charlottesville, VA 22901
3	Commander US Army Armament Materiel Readiness Command ATTN: Joint Army-Navy- Air Force Conventional Ammunition Prof Coord Gp/E. Jordan Rock Island, IL 61201	1	Commander US Army TRADOC Systems Analysis Activity ATTN: ATAA-SL (Tech Lib) White Sands Missile Range New Mexico 88002
		1	Deputy Assistant Secretary of the Army (R&D) ATTN: Asst for Rsch Washington, DC 20310

56

DISTRIBUTION LIST

No. of Copies	Organization	No. of Copies	Organization
1	Commander US Army Research Office P.O. Box 12211 Research Triangle Park North Carolina 27709	1	US Naval Civil Engineering Laboratory ATTN: Dr. W. A. Shaw Fort Hueneme, CA 93403
2	US Army Engineer Waterways Experiment Station ATTN: Library, Mr. W. Flateau P.O. Box 631 Vicksburg, MS 39180	1	Commander US Naval Civil Engineering Lab ATTN: Library Port Hueneme, CA 93401
2	Commander David W. Taylor Naval Ship Research & Develop. Center ATTN: Dr. W. W. Murray, Code 17 Dr. G. Everstine, Code 1844 Bethesda, MD 20084	1	Commander US Naval Research Laboratory ATTN: Code 2027, Tech Lib Washington, DC 20375
2	Commander US Naval Surface Weapons Center ATTN: Mr. J. C. Talley Dr. W. Soper Dahlgren, VA 22448	2	Superintendent US Naval Postgraduate School ATTN: Tech Reports Sec. Code 57, Prof. R. Ball Monterey, California 93940
1	Commander US Naval Surface Weapons Center ATTN: Dr. P. Huang Silver Spring, MD 20910	2	AFATL (ATRD, R. Brandt) Eglin AFB, AL 32542
1	Commander US Naval Surface Weapons Center ATTN: Code 241 (Mr. Proctor) Silver Spring, MD 20910	3	AFWL/WLTL (DYT/MAJ G. Ganong; DYT/Mr. Charles Needham; DYT/CPT D. Marten) Kirtland AFB, NM 87117
1	Commander US Naval Weapons Center ATTN: Code 6031, Dr. W. Stronge China Lake, CA 93555	1	AFML (MAMD, Dr. T. Nicholas) Wright-Patterson AFB Ohio 45433
1	Commander US Naval Ship Research and Development Center Facility ATTN: Mr. Lowell T. Butt Underwater Explosions Research Division Portsmouth, VA 23709	2	AFFDL (FDTR, Dr. F. J. Janik, Jr.) (FBE, Mr. R. M. Bader) Wright-Patterson AFB Ohio 45433
		2	Director Los Alamos Scientific Lab. ATTN: Docu Con P.O. Box 1663 Los Alamos, NM 87544

DISTRIBUTION LIST

No. of Copies	Organization	No. of Copies	Organization
1	Director Lawrence Livermore Laboratory Technical Information Division P.O. Box 808 Livermore, CA 94550	1	Kaman Sciences Corporation ATTN: Dr. D. Sachs 1500 Garden of the Gods Road Colorado Springs, CO 80907
4	Sandia Laboratories ATTN: Info Distr Division Dr. W. Herrmann Dr. S. W. Key Mr. R. D. Krieg Dr. W. A. Von Riesemann Albuquerque, NM 87115	1	Systems, Science and Software ATTN: Dr. J. K. Dienes P.O. Box 1620 LaJolla, CA 92037
1	Computer Code Consultants ATTN: W. Johnson 527 Glencrest Drive Solona Beach, CA 92075	1	Lovelace Foundation ATTN: Dr. D. Richmond 4800 Gibson Blvd, S.E. Albuquerque, NM 87100
2	Battelle Columbus Laboratories ATTN: Dr. L. E. Hulbert Mr. J. E. Backofen, Jr. 505 King Avenue Columbus, Ohio 43201	1	Massachusetts Institute of Technology Aeroelastic and Structures Research Laboratory ATTN: Dr. E. A. Witmer Cambridge, MA 02139
1	Factory Mutual Research Corp. ATTN: Mr. Robert Zalosh 1511 Boston-Providence Turnpike Norwood, MA 02062	1	Ohio State University Department of Engineering Mechanics ATTN: Prof. K. K. Stevens Columbus, Ohio 43210
1	General Electric Company, TEMPO 7800 Marble N.E. Albuquerque, NM 87110	3	Southwest Research Institute ATTN: Dr. W. Baker P. S. Westine J. C. Hokanson P.O. Drawer 28510 San Antonio, Texas 78284
1	J. G. Engineering Research Associates 3831 Menlo Drive Baltimore, MD 21215	2	Stanford Research Institute ATTN: Dr. Herbert E. Lindberg Dr. G. R. Abrahamson 333 Ravenswood Avenue Menlo Park, California 94025
1	Kaman-Avidyne ATTN: Dr. N. P. Hobbs 83 Second Avenue Northwest Industrial Park Burlington, MA 01803	1	University of Delaware Department of Mechanical and Aerospace Engineering ATTN: Prof. J. R. Vinson Newark, Delaware 19711

DISTRIBUTION LIST

Aberdeen Proving Ground

Cdr, USAEA
  ATTN: SAREA-MT-T, Mr. R. Thresher
Marine Corps Ln Ofc
Dir, USAMSAA
  ATTN: Dr. J. Sperazza
         Mr. R. Norman, WSD